Applied Physics Reviews

REVIEW ARTICLE | APRIL 19 2022

2D materials-enabled optical modulators: From visible to terahertz spectral range

Xuetao Gan ; Dirk Englund ; Dries Van Thourhout ; Jianlin Zhao

Appl. Phys. Rev. 9, 021302 (2022)
https://doi.org/10.1063/5.0078416

Applied Physics Reviews REVIEW scitation.org/journal/are

2D materials-enabled optical modulators: From visible to terahertz spectral range

Cite as: Appl. Phys. Rev. 9, 021302 (2022); doi: 10.1063/5.0078416
Submitted: 12 November 2021 · Accepted: 15 March 2022 ·
Published Online: 19 April 2022

View Online Export Citation CrossMark

Xuetao Gan,[1,a)] Dirk Englund,[2] Dries Van Thourhout,[3,4] and Jianlin Zhao[1]

AFFILIATIONS

[1]Key Laboratory of Light Field Manipulation and Information Acquisition, Ministry of Industry and Information Technology, and Shaanxi Key Laboratory of Optical Information Technology, School of Physical Science and Technology, Northwestern Polytechnical University, 710129 Xi'an, China
[2]Research Laboratory of Electronics, Massachusetts Institute of Technology, Cambridge, Massachusetts 02139, USA
[3]Photonics Research Group, INTEC, Ghent University-IMEC, Ghent B-9000, Belgium
[4]Center for Nano-and Biophotonics (NB-Photonics), Ghent University, Ghent B-9000, Belgium

[a)]Author to whom correspondence should be addressed: xuetaogan@nwpu.edu.cn

ABSTRACT

Two-dimensional (2D) materials with layered structures have a variety of exceptional electronic and optical attributes for potentially developing basic functions of light wave technology from light-emitting to -modulating and -sensing. Here, we present state-of-the-art 2D materials-enabled optical intensity modulators according to their operation spectral ranges, which are mainly determined by the optical bandgaps of the 2D materials. Leveraging rich electronic structures from different 2D materials and the governed unique light–matter interactions, the working mechanisms and device architectures for the enabled modulators at specific wavelength ranges are discussed. For instance, the tunable excitonic effect in monolayer transition metal dichalcogenides allows the modulation of visible light. Electro-absorptive and electro-refractive graphene modulators could be operated in the telecom-band relying on their linear dispersion of the massless Dirac fermions. The bendable electronic band edge of the narrow bandgap in few-layer black phosphorus promises the modulation of mid-infrared light via the quantum-confined Franz–Keldysh or Burstein–Moss shift effect. Electrically and magnetically tunable optical conductivity in graphene also supports the realizations of terahertz modulators. While these modulators were demonstrated as proof of concept devices, part of them have great potential for future realistic applications, as discussed with their wavelength coverage, modulation depth, insertion loss, dynamic response speed, etc. Specifically, benefiting from the well-developed technologies of photonic chips and optical fibers in telecom and datacom, the 2D materials-based modulators integrated on these photonic structures are expected to find applications in fiber and chip optical communications. The free-space mid-infrared and terahertz modulators based on 2D materials can expect application in chemical bond spectroscopy, free-space communications, and environment/health sensing.

TABLE OF CONTENTS

I. INTRODUCTION

Optical modulators play a crucial role in optical information processing systems, including optical communication, interconnect, computing, and sensing, etc. In the operations, modulations of a light beam could be realized by altering its amplitude, phase, or polarization via the variations of absorption or refractive index of optical materials. According to the actuation methods, optical modulators are typically

developed with the electro-optic, acoustic-optic, magneto-optic, thermo-optic, all-optical effects, and mechanical deformations. There are a variety of commercial optical modulators manufactured with mature technologies, and the active media are normally chosen from semiconductors, ferroelectric oxides, ferromagnetic oxides, liquid crystals, etc. For example, lithium niobate-based modulators exploit its linear electro-optic effect to achieve low-power consumption and high-speed operation, which have been widely employed in high-speed optical communications and microwave photonics.[1,2] To be complementary with the on-chip optical interconnects, reliable optical modulators are integrated onto silicon photonic chips using silicon's strong thermo-optic and plasma dispersion effects, which enable reconfigurable integrated photonic devices and single-chip microprocessor communicated directly with light.[3–5]

Recently, two-dimensional (2D) materials with layered structures have emerged as an attractive active medium for constructing optoelectronic devices.[6–14] It has been reported that versatile single-elementary and compound materials have layered stacking forms, which could be exfoliated into a 2D material with a thickness of few-atom layer. Therefore, plentiful electrical, optical, magnetic, and mechanical properties could be acquired from 2D materials.[15–21] These physical attributes provide possibilities to modulate optical signals via various mechanisms with 2D materials. The family of 2D materials has a rich variety of electronic properties, including semi-metallic graphene, insulating boron nitride (BN), semiconducting transition metal dichalcogenides (TMDCs), and black phosphorus.[22–26] Determined by this, the optical responses of 2D materials could span a broad region of the electromagnetic spectrum,[15,27–30] ranging from microwave to ultraviolet wavelengths, as schematically shown in Fig. 1. In addition, their optical bandgaps could be engineered by controlling the layer numbers, alloy compositions, or stacking behaviors of heterostructures.[31–36] Relying on these electrical and optical properties, it is possible to fabricate electro-optic modulators in 2D materials operating over a broad spectral range by employing the quantum confined Franz–Keldysh effect and Pauli-blocked Burstein–Moss shift effect.[37–39] The quantum confined carrier dynamics and small substance volume in 2D materials also promise strong modifications of their optical responses under optical radiations by injecting high-density photon-generated carriers, enabling the all-optical modulations.[40–42] 2D materials also harbor ferromagnetism with high transition temperatures to support optical modulators with the magneto-optic effect.[43–45] Even for the insulating BN without ferromagnetism or ferroelectricity, its polar crystal structure could be exploited to excite the phonon polaritons for high efficient acoustic-optical modulation.[46,47]

2D materials also have other unique attributes to endow their benefits in applications of optical modulators. While there are only mono- or few-atomic-layer thickness, light–matter interactions in 2D materials are extremely strong due to the reduced dielectric screening and effective many-body interaction. For instance, graphene monolayers absorb the single-passed light with an efficiency of 2.3% over a wavelength range from visible to mid-infrared.[48,49] Molybdenum disulfide (MoS_2) monolayers could yield an absorption coefficient of ~10% around the excitonic resonances.[50–52] The ultrathin flakes with reduced dielectric screening also allow easy tuning of their electrical and optical properties via electrostatic field, chemical doping, strain, and pressure,[53–59] which are difficult to realize in bulk materials. In addition, 2D materials' surfaces are naturally passivated without any dangling bonds.[60–62] It is possible to construct vertical heterostructures using different 2D materials via the weak van der Waals force, which thereby gets rid of issues of lattice mismatch and enables band

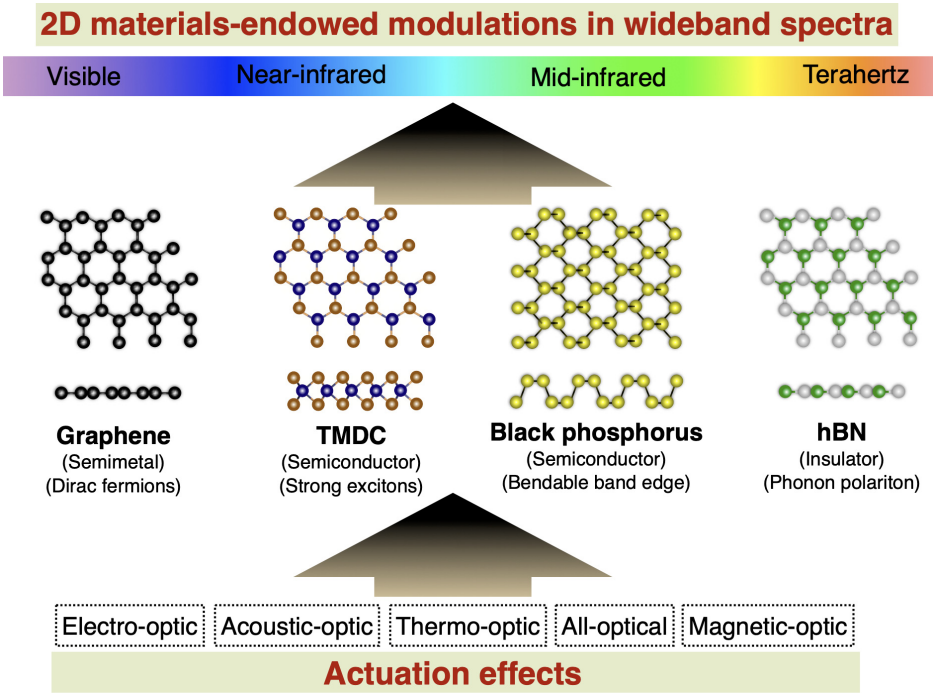

FIG. 1. 2D materials-enabled optical modulators could operate in various spectral ranges from visible to terahertz benefiting from rich electronic structures in 2D materials and the governed unique light–matter interactions, which are actuated by electro-optic, acoustic-optic, thermo-optic, all-optical, and magnetic-optic effects.

structure engineering.[33,63] This also facilitates the integrations of 2D materials with photonic elements or chips, ensuring that the integrated optical modulators be applied in wide areas.[64]

In this Review, we present the state-of-the-art 2D materials-based optical modulators according to their operation spectral ranges, which are mainly determined by the optical bandgaps of the 2D materials. For example, graphene's zero-bandgap and linear dispersion endow electro-optic modulations over a range from visible to terahertz band; electro-optic modulators of TMDCs or black phosphorus have operation wavelength ranges from visible to mid-infrared due to their limited bandgaps. In addition, in those 2D materials, the main contributions of light–matter interactions arise from different physical mechanisms, including the strong many-body interactions, tunable band structures of quasi-2D electron gas, etc. Wherein the working principles of those 2D materials-based optical modulators will be illustrated carefully, their modulations on optical intensity are considered as the scope of this review. In addition, integrations of those modulators with various photonic structures are discussed as well, such as on-chip waveguides, resonators, plasmonic nanoantenna, and optical fibers. The photonic structures could enhance light–matter interactions in 2D materials significantly to get over the drawback caused by their intrinsically ultrathin material substance, which facilitates the high modulation performances. On the other hand, those well-studied photonic structures provide mature platforms for carrying out electro-optic, thermo-optic, all-optical effects in 2D materials. Considering the well-developed technologies of photonic chips and optical fibers are mainly exploited in optical telecom and datacom, the discussions of 2D materials-based modulators integrated on them will focus on the possible applications in optical communications. For the 2D materials-based modulators operated in the mid-infrared and terahertz wavelength ranges, the 2D materials were normally integrated with plasmonic structures to enhance light–matter interactions and the resulted modulators were operated in the free-space configuration for potential applications in chemical bond spectroscopy, free-space communications, environment/health sensing, etc. The corresponding performance merits evaluated on these modulators will mainly include the wavelength coverage, modulation depth, insertion loss, dynamic response speed, etc.

II. EXCITONIC MODULATION OF VISIBLE LIGHT IN THE TMDCS MONOLAYER

Group-VI TMDC monolayer, MX_2 (M = Mo, W; X = S, Se, Te), have received great research interest due to their strong photoluminescence (PL),[31,65–67] current on–off ratios exceeding 10^8 in field-effect transistors,[68] and efficient valley and spin control by optical helicity.[69–72] In a TMDC monolayer, a single layer of transition metal atoms is sandwiched between two layers of chalcogen atoms in the trigonal prismatic structure, as shown in Fig. 2(a). It has out-of-plane mirror symmetry and broken in-plane inversion symmetry. Their bulk materials are commonly stacked by monolayers in the ABAB… sequence, forming 2H polytype, which have inversion symmetry and

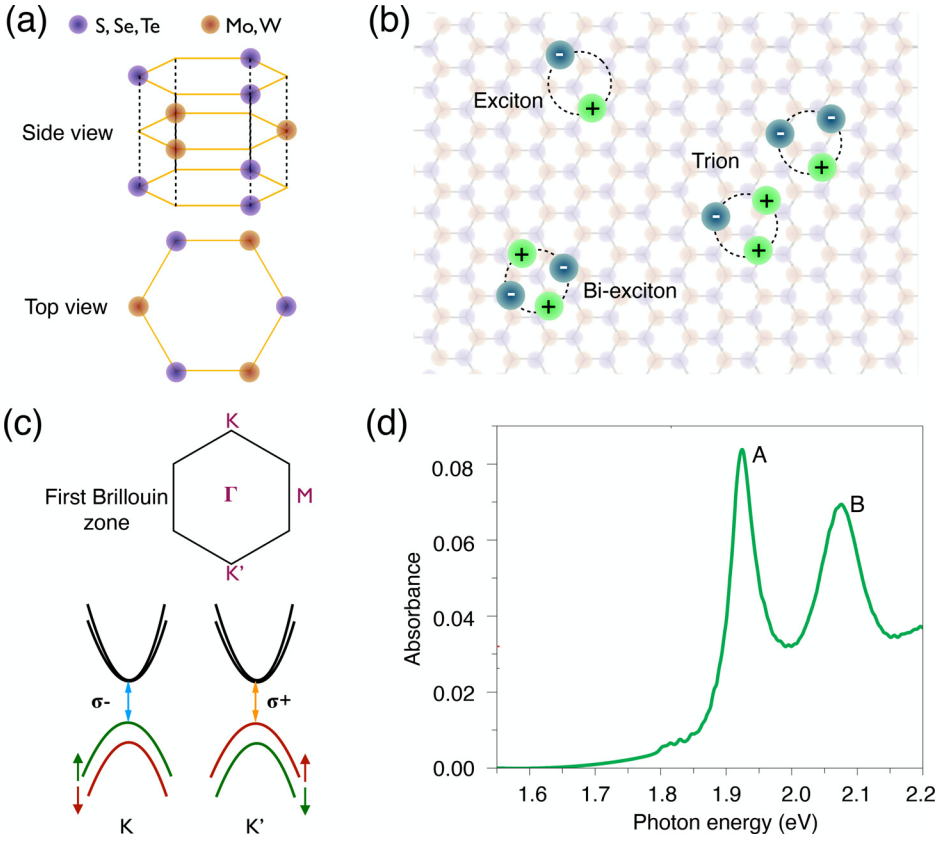

FIG. 2. (a) Schematic of the trigonal prismatic structure of a monolayer TMDC. (b) Illustration of a two-particle charge-neutral exciton, two three-particle trions, and a four-particle bi-exciton. (c) Simplified picture of the electronic bands near the K and K′ points of the Brillouin zone, which are spin–split by the spin–orbit interactions. (d) Absorption spectrum of monolayer MoS_2 with two prominent resonance peaks, known as the A and B excitons. Reproduced with permission from Mak *et al.*, Nat. Mater. **12**, 207 (2013). Copyright 2013 Nature Publishing Group.

indirect bandgap. In contrast to graphene, TMDC monolayers have direct bandgaps in the near-infrared and visible wavelength regions.[9]

Because of the reduced dielectric screening and relatively heavy particle band masses associated with the Mo or W *d*-orbitals, charge carriers in TMDC monolayers have strong Coulomb interactions to form tightly bound excitons, trions, and bi-excitons [Fig. 2(b)].[51,73,74] The binding energies of excitons are reported to vary from 0.5 to 1 eV, which are nearly one order of magnitude larger than those found in conventional quasi-2D systems.[51,67] These many-body oscillators are so robust that they could be clearly resolved at room temperature. Even with a relatively high carrier density, TMDC monolayers are still strong many-body interacting systems. By injecting carriers into or dissipating carriers from the TMDC monolayers, it is easy to switch the many-body oscillators among these states. With that, desirable modulation of excitonic optical responses in TMDC monolayers are expected, such as photoluminescence, absorption, and reflection. In addition, as shown in Fig. 2(c), the edge of the direct bandgap locates at the K (and K′) point of the Brillouin zone. The large spin-orbital interaction splits the highest valence bands at the K (and K′) point by 0.16 eV,[69] which also lifts their spin degeneracy. The lack of inversion symmetry in TMDC monolayers results in couplings of valley and spin degrees, which allows the optically controlled single valley and spin via circularly polarized light.[69,75–77] This attribute provides another degree to modulate the optical signal using TMDC monolayers.[78]

The robust exciton behaviors in TMDC monolayers enable its strong interactions with the on-resonance optical radiations even at room temperature. The solid line in Fig. 2(d) displays the experimentally measured optical absorption spectrum from an undoped MoS_2 monolayer.[51] Two pronounced absorption peaks are observed, corresponding to the excitonic transitions from the highest spin–split valence bands to the lowest conduction bands, known as the A and B excitons. They are modified significantly by the strongly bounded excitons. The absorbance could be high as 10% even only with a monolayer material. In contrast to what expected in a 2D system without the excitonic effect, this measured absorption should have a step-function-like spectrum originated from the energy-independent joint-density-of-states and transition matrix elements near parabolic band edges. By modifying the charge doping level in the TMDC monolayer, the exciton could be charged by binding an additional electron or hole to form a tightly bound trions,[79] which decreases the density of excitons. The trion's transition provides another on-resonance channel for strongly enhanced light–matter interaction. By switching the oscillating strength between excitons and trions in TMDC monolayers using electrical or chemical doping, the resonant optical responses could be modified readily.

As shown in Fig. 3(a), a back-gated field-effect transistor device could be constructed to apply a vertical electrostatic field across the MoS_2 monolayer. With different gate voltages (V_g), representative absorption and PL spectra of the MoS_2 monolayer were acquired, as shown in Figs. 3(b) and 3(c), respectively.[51] Because of intrinsic doping by the substrate, the charge neutrality of the MoS_2 monolayer was obtained around $V_g = -70$ V. There are two absorption peaks with values close to 8% around the photon energies of 1.9 and 2.05 eV, which are related to the two excitons determined by the spin-split valence bands. As V_g increases to 80 V gradually, the high doping density in the MoS_2 monolayer would charge the excitons into trions, which, therefore, reduces the two absorption peaks greatly to 4% and 6%, respectively. On the other hand, the increased trion density results in the observable absorbance around the photon energy of 1.85 eV (~3%). Corresponding to the electrically controlled switching between excitons and trions, the variations of PL emissions are displayed in Fig. 3(c). Thanks to large binding energies of excitons and trions, these electrically modified absorptions could be clearly distinguished even at room temperature. This facilitates realistic applications of exciton-based optoelectronic devices in TMDC monolayers. Of course, much narrower linewidths of absorption and PL peaks could be obtained at lower temperatures for understanding the many-body physics.

An exciton-based electro-optic modulator of the MoS_2 monolayer was proposed and fabricated by Fang *et al.*,[80] which was combined with a plasmonic nanostructure, as shown in Fig. 4(a). Surface plasmons of metallic nanostructures have extremely high density of photon states in a nanoscale. The few atomic layers of the MoS_2 monolayer allows its tightly spatial overlap with the surface plasmon after its integration with the metallic nanostructures. If the photon energies in the monolayer's exciton and plasmon are coincident as well, the two quasiparticle would realize a strong coupling to form exciton–plasmon polariton, which is also called "plexciton." Considering the electrical tunability of MoS_2 exciton, the state of plexciton resonance could be employed as modulator.

To make the device, a MoS_2 monolayer was mechanically exfoliated onto a silicon substrate covered with 300 nm thick silicon oxide

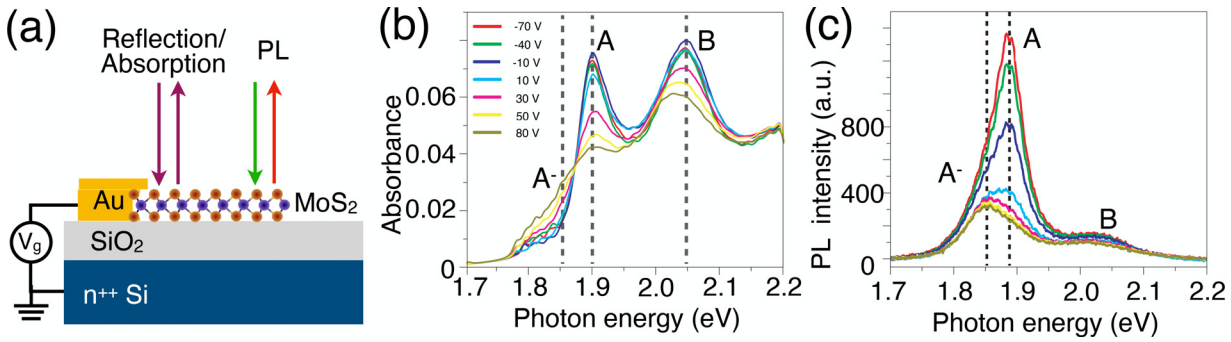

FIG. 3. (a) Schematic of gated monolayer MoS_2 for tuning its absorbance and PL. (b) Variation of absorbance measured from gated monolayer MoS_2 at different voltages. (c) Electrically controlled oscillations between exciton and trion emissions. Reproduced with permission from Mak *et al.*, Nat. Mater. **12**, 207 (2013). Copyright 2013 Nature Publishing Group.

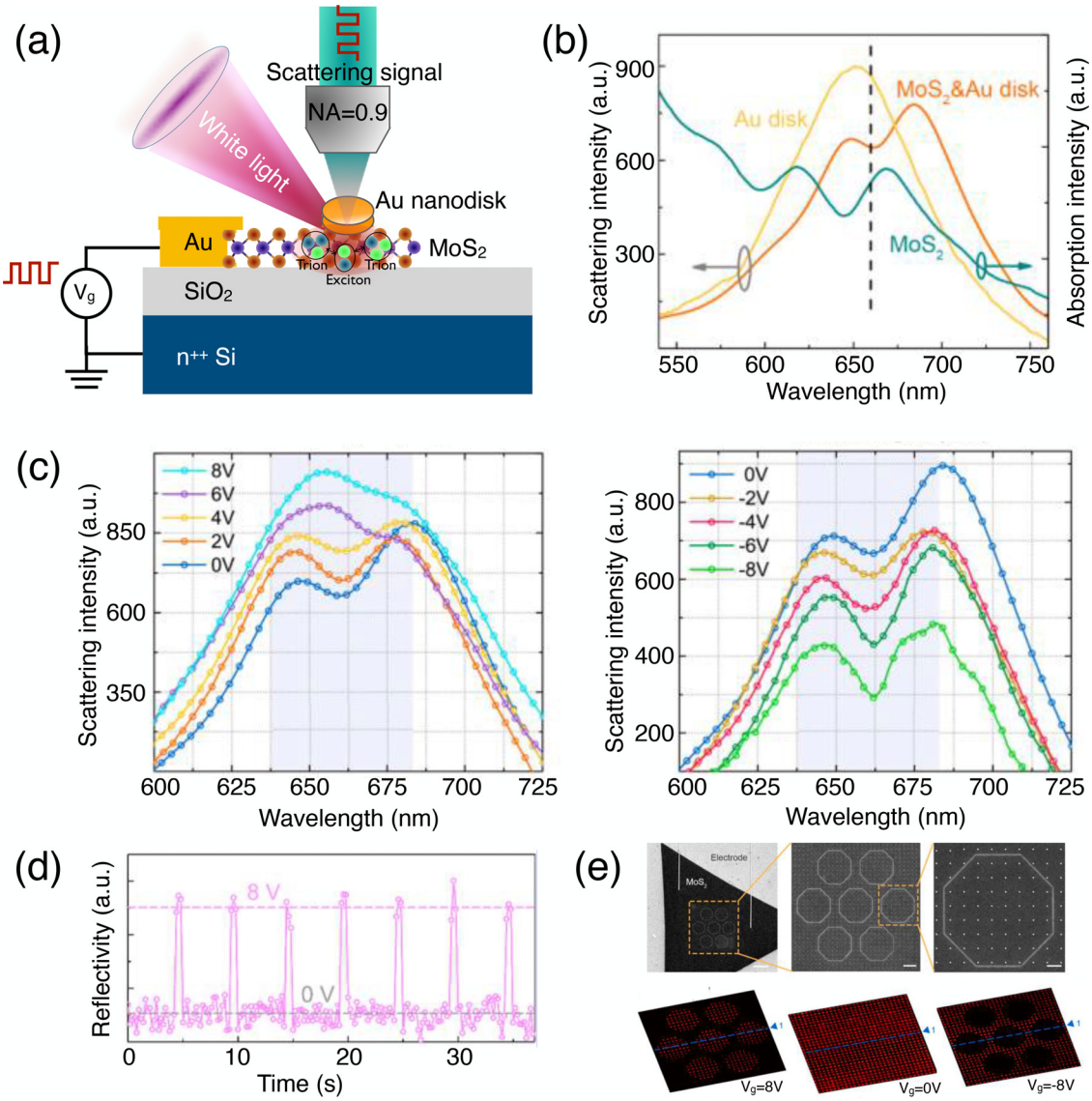

FIG. 4. (a) Schematic of the electro-optic modulator based on the exciton-plasmon polaritons by modulating the exciton in monolayer MoS_2 coupled with an Au nanodisk. (b) Scattering spectra of Au nanodisk, MoS_2–Au nanodisk, and absorption of the monolayer MoS_2, indicating the formation of exciton–plasmon polariton. (c) Variations of the scattering signals from the MoS_2–Au nanodisk when different gating voltages were applied. (d) Time response of the MoS_2–Au nanodisk electro-optic modulator. (e) Electrically controlled display by modulating an array of MoS_2–Au nanodisks. Reproduced with permission from Li *et al.*, ACS Nano **11**, 9720 (2017). Copyright 2017 American Chemical Society.

(SiO_2). A metal electrode was deposited on MoS_2 to implement the back-gate via the silicon substrate. A gold nanodisk with a radius of 60 nm and a thickness of 30 nm was fabricated on top of the MoS_2 monolayer by electron beam lithography and metal deposition. The scattering spectrum of a bare gold nanodisk presents a Lorentzian-type resonance peak around 650 nm, which is close to the exciton resonance of the MoS_2 monolayer, as displayed in Fig. 4(b). The integration of the MoS_2 monolayer modifies the scattering spectrum of the gold nanodisk into an asymmetric Fano-type resonance with a dip at the exciton wavelength, indicating the coherent coupling between the exciton and plasmon. By electrically gating the MoS_2 monolayer with different voltages, the scattering spectra of the MoS_2-nanodisk were modulated, as shown in Fig. 4(c). Increasing V_gs from 0 to 8 V, the dip of the Fano-resonance line shape increases gradually. It could be attributed to the suppression of exciton-enhanced absorption in the MoS_2 monolayer after the carrier doping. Around the wavelength of 685 nm, the scattering intensities reduce as the voltage increases since the trion-related absorption becomes prominent with the charged exciton. If negative voltages were applied (from 0 to −8 V), the scattering dips of the Fano-resonance become much deeper as more trions are

decharged into excitons. By comparing the scattering spectra obtained under $V_g = 0$ and 8 V, the modulation depth of the varied scattering intensities around the resonance wavelength is ~47.6%. The electro-optic response time of the exciton-plasmon modulator was exploited further by applying a series of squared electrical voltage pulses in milliseconds. The reflection signal around the exciton resonance was switched successfully when the applied V_g varied between 0 and 8 V, showing a response time less than 200 ms, as shown in Fig. 4(d). The slow modulation speed is limited by the long integration time of the signal-processing camera. The ultimate response speed is actually determined by the *RC* constant of the parallel plate capacitor composed of the MoS_2 monolayer and silicon back-gate (estimated as ~50 ns). Based on this gate-dependent exciton–plasmon coupling, a 2D display device could also be constructed by patterning an array of nanodisks on a chemical vapor deposition-grown MoS_2 monolayer [Fig. 4(e)], as detailed in Ref. 80.

According to the Lorentz oscillator model, optical responses of TMDC monolayers on-resonance with exciton not only present strongly enhanced optical absorption but also have great dispersion of the refractive index. It was reported that the refractive index of the MoS_2 monolayer could be higher than 6.5 at the visible spectral range,[52] leading to potential applications for making ultrathin and ultracompact optical elements. For instance, Lu *et al.* reported the world's thinnest optical lens and high-efficiency gratings using mono- and few-layer of MoS_2.[81] If the MoS_2 layers were electrically gated, the lens or gratings would become active optical devices. In 2018, Park *et al.* and Imamoglu *et al.* separately reported that a $MoSe_2$ monolayer has a high level of reflectance.[82,83] With different substrates, the monolayer mirror has a reflectivity up to 85% and 41%, respectively. From a view of quantum electrodynamics, the $MoSe_2$ monolayer provides an array of electrical dipoles. With an optical excitation, the dipoles are driven to oscillate and re-radiate light at the same wavelength of the incident light. Both forward and backward radiations are obtained with respect to the direction of the incident light. A perfect mirror would be realized when the forward radiations destructively interfere with the incident wave, resulting in zero transmission. The excellent coherent properties of excitons in the $MoSe_2$ monolayer provide the homogenous distributions of dipoles to ensure the completely destructive interference between the incident wave and exciton re-radiation.[84] Electrical tuning of the exciton oscillator strength, therefore, promises a switchable mirror. As shown in Figs. 5(a) and 5(b), a $MoSe_2$ monolayer was encapsulated between two hexagonal BN layers and contacted with an electrode.[82] Combined with the highly doped silicon substrate, the $MoSe_2$ layer functions as one planar electrode of the parallel plate capacitor, which has a 285 nm thick SiO_2 dielectric layer. With V_g applied to the silicon back gate, the carrier densities in $MoSe_2$ can be tuned readily. Figure 5(c) displays the reflection images under the on-resonance illumination with V_gs of –20 and 30 V, respectively. From the intrinsic $MoSe_2$ layer ($V_g = -20$ V), its reflection in contrast to the substrate was observed substantially. It disappeared in an

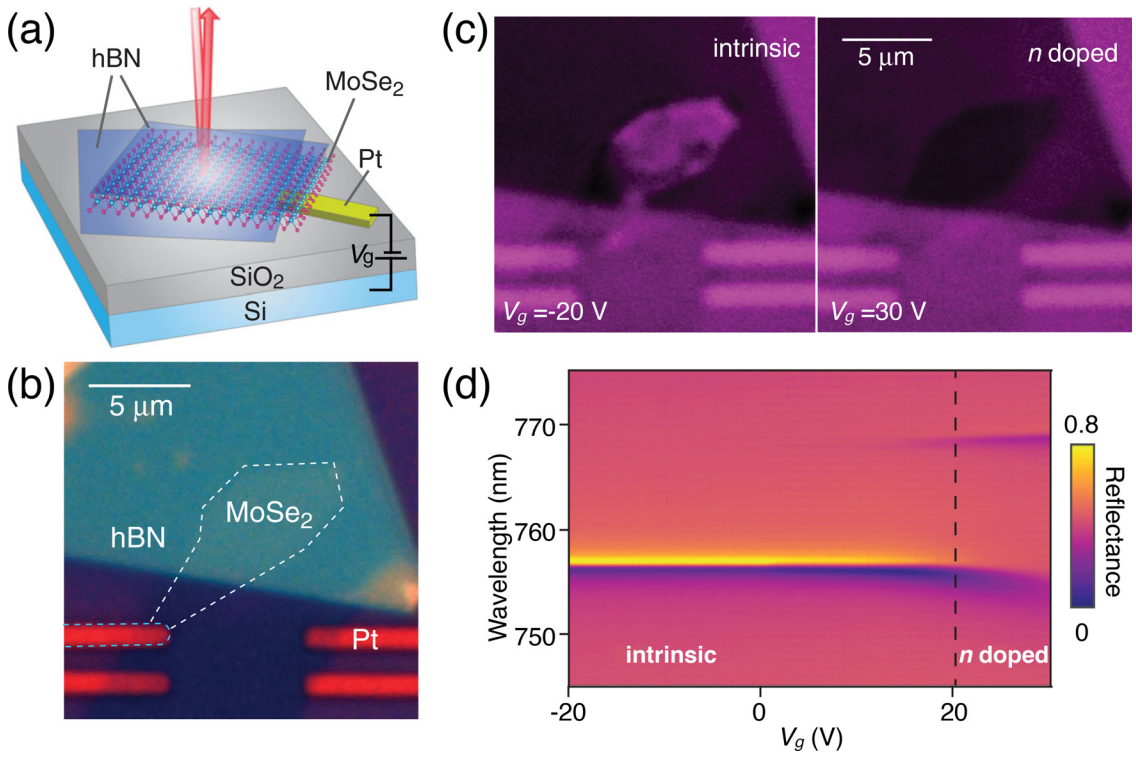

FIG. 5. (a) Schematic of a monolayer $MoSe_2$ mirror, which could be electrically switched by the back gating. (b) Optical microscopic image of the electrically tuned mirror, including a monolayer $MoSe_2$ sandwiched by two BN layers and contacted with a Pt electrode. (c) Reflection images of the mirror device under 750 nm on-resonance laser illumination with V_g of –20 and 30 V. (d) Reflection spectra of a monolayer $MoSe_2$ mirror at different V_g values. Reproduced with permission from Scuri *et al.*, Phys. Rev. Lett. **120**, 37402 (2018). Copyright 2018 American Physical Society.

n-doped $MoSe_2$ layer ($V_g = 30$ V). From the gate-voltage dependent reflection spectra shown in Fig. 5(d), one can find at $V_g = 30$ V that there is a trion-related reflection peak due to the charging of excitons. The reflection spectrum becomes flat around the wavelengths of the exciton. Here, the reflection peaks around the exciton have asymmetric Fano-type lineshapes originating from the interference of separated reflections from the $MoSe_2$ monolayer and back silicon substrate. In the work reported by Imamoglu *et al.*, the driven voltages for realizing the maximum variation of the reflection intensity are much smaller benefiting from the thin dielectric film of the 33 nm thick BN layer. The modulation depth of the reflection intensity was estimated around 80% on the exciton resonance with an actuated voltage of 2 V.[83] Though the dynamic responses of the demonstrated $MoSe_2$ modulators were not demonstrated, a subnanosecond timescale is expected by engineering the device with a small capacitance as well as the intrinsic low resistance Ohmic contacts of the $MoSe_2$ monolayer.[85]

These strong exciton-photon interactions in the TMDC monolayers have great potential to improve modulators with high-efficiency. Furthermore, the light-matter coupling in the TMDC monolayers could be enhanced further by integrating them with photonic structures to employ resonance and waveguiding modes, including photonic crystal cavities, waveguides, and microrings,[86–89] which are attractive for chip-integrated optical modulators. In addition, since the lifetimes of excitons are in the scale of picoseconds, it is possible to carry out ultrafast operations in the exciton-based modulator. Note that exciton's quasiparticle properties with weak dielectric screening make it only respond to light waves in a narrowband range, which makes it negative to perform as a broadband optical modulator. On the other hand, TMDC monolayers have large optical bandgaps. This limits the spectral range of TMDC modulators to visible and near-infrared spectral range. For instance, as one of the monolayer TMDCs with the smallest bandgap, the $MoTe_2$ monolayer has a bandgap still larger than 1.1 eV.[67] While thicker $MoTe_2$ has smaller bandgap around 1 eV,[90] it loses the behavior of tightly bound exciton, which would degrade its optical response significantly. As an alternative routing, doping TMDC monolayers at wavelengths far from its exciton resonance could also be employed to carry out a modulator based on the electro-refractive response. While the modulation depths of this off resonance modulator were not expected to be as high as those governed by the exciton-modulated one, it could perform with negligible insertion loss and broad bandwidth.[91,92]

Optical modulators in the visible spectral range are essential for the applications of virtual-reality displays, visible light communication, and optogenetics, etc. The state-of-the-art visible modulators were normally realized by the technologies of the liquid crystal or micro-electromechanical system, which have the disadvantages of slow operation speed, large operation voltages, and complex and bulky systems.[93] Though the reported modulators based on TMDC monolayers are still in the state of proof of principle, they have the potential to solve some of the problems. For example, by mechanically stacking TMDC monolayers with BN and graphene via their van der Waals forces, the modulators of TMDC monolayers could be constructed with a thickness of few-atomic layers, which promise the device with high compactness and integration level. As discussed above, because the operations of the TMDCs-based modulators are governed by the electrical actuations of the parallel capacitors, the dynamic response speed could approach GHz. Note that to guarantee the future realistic applications of these modulators, their modulation depth should be improved further, such as integrating with nanophotonic structures to enhance the light-TMDCs interactions.

III. GRAPHENE OPTICAL MODULATORS OPERATING AT TELECOM-BAND

With the rapid development of optical communications and data communications, high-performance optical modulators operating in telecom-band encounter a variety of challenges in power consumption, optical bandwidth, dynamic response, modulation depth, etc. Strong light–matter interactions, unique electrical properties, and the ease-of-integration in 2D materials have the potential to solve these problems. Because electronic bandgaps of TMDCs mismatch with the photon energy of the telecom-band light wave, graphene is considered to be a suitable material for modulations in the telecom-band relying on its broadband optical responses from ultraviolet to terahertz band. In addition, compared with TMDCs, graphene's wafer-scale synthesis and transfer with high qualities are well developed, which paves the way for real applications of graphene modulators. In this section, we mainly discuss the promise of graphene modulators for telecommunications. Since the telecommunication systems are mainly built on the optical fibers and photonic integrated chips, the reported graphene modulators in the telecom-band were mainly carried out with chip-integration or fiber-integration. These integrations could also enhance the light–graphene interactions with optical waveguides or resonators to facilitate the improvement of modulation performances. In Secs. III and IV, graphene-based mid-infrared and terahertz modulators will be involved, which were implemented in the free-space configuration by integrating graphene with plasmonic structures or patterning graphene with a plasmonic resonance response to enhance light–graphene interactions. While visible free-space graphene modulators were also reported,[94] there are unfortunately some disadvantages of requiring high operation voltages for tuning the Fermi level and large insertion loss. They will not be discussed here.

A. On-chip graphene electro-absorptive modulators

In the visible to mid-infrared range, graphene's optical absorbance is primarily attributable to interband transition, which is a constant value determined by the fine-structure constant in pristine graphene.[49] However, if a vertical electrostatic field is applied over graphene, the increased carrier density would shift the Fermi level (E_F) and induce Pauli blocking of the optical transition,[53,95] as schematically shown in Fig. 6(a). For the telecom-band light wave with photon energy around $h\nu_0 = 0.8$ eV, E_F tuning larger than 0.4 eV would contribute to the reduced absorption, giving rise to an electro-absorptive modulator.

With this principle of operation, Liu *et al.* transferred a graphene layer onto a silicon waveguide to fabricate the first graphene-based modulator.[39] Since the graphene layer is single atomic thin, it cannot couple with the surface illumination effectively. Its integration with an optical waveguide extends the light-graphene coupling length, resulting in reliably increased optical attenuation from 0.1 to about 10 dB.[96,97] By electrically suppressing graphene's absorption, a modulator with a high extinction ratio could be realized. As schematically shown in Fig. 6(b), to electrically gate the graphene layer, an electrical capacitor was built with the graphene layer and the silicon waveguide as two plate electrodes. Figure 6(c) displays the scanning electron microscopic (SEM) image of the fabricated device. Graphene

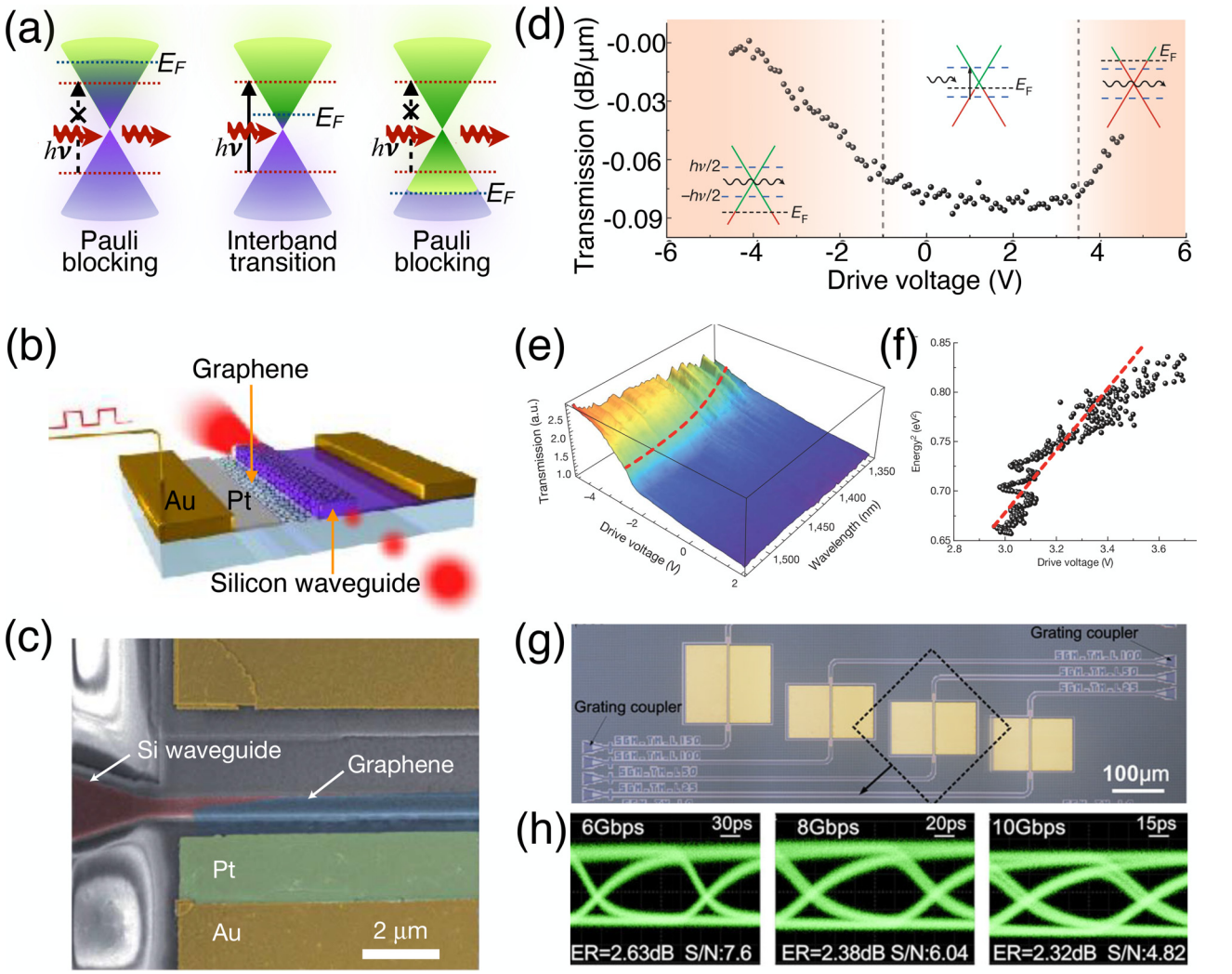

FIG. 6. Broadband graphene electro-absorptive modulators integrated on silicon waveguides. (a) Band structures of graphene at different doping levels, where graphene becomes transparent when the interband transition is Pauli blocked, as shown in the left and right images. (b) Schematic representation of a waveguide-graphene modulator, where the graphene and silicon waveguides are separated by a thin alumina layer to form a parallel capacitor. (c) SEM image of a fabricated device. (d) Static electro-optic response of the device shown in (c) at different drive voltages. (e) Transmission spectra of the device shown in (c) at different drive voltages. (f) Squared photon energy vs critical drive voltage for maximum transmission change rate extracted from (e). (g) Optical microscopic images of several graphene electro-absorptive modulators integrated on a CMOS silicon photonic chip. (h) Optical eye diagrams measured at 1560 nm for one of the devices shown in (g) at 6, 8, and 10 Gb/s modulation speeds. (b)–(f) Reproduced with permission from Liu *et al.*, Nature 474, 64 (2011). Copyright 2011 Nature Publishing Group. (g)–(h) Reproduced with permission from Hu *et al.*, Laser Photonics Rev. **10**, 307 (2016). Copyright 2016 Wiley-VCH Verlag GmbH & Co. KGaA.

transferred onto the silicon waveguide was selectively etched to cover the waveguide. A 7-nm-thick alumina was inserted into them to work as the dielectric spacer. The silicon waveguide was electrically connected by a 50-nm-thick silicon layer. The modulation performance was implemented by measuring the waveguide transmission of light at 1530 nm by applying different V_gs, as shown in Fig. 6(d). At low applied voltages ($-1\,\mathrm{V} < V_g < 3.8\,\mathrm{V}$), graphene's Fermi level is close to the Dirac point. Its strong light absorption induces a quite low transmission of the hybrid graphene-waveguide. For high drive voltages, the Fermi level was tuned to a level of $h\nu_0/2$ lower (higher) than the Dirac point, Pauli blocking of the interband transition forbids the optical absorption of graphene, giving rise to waveguide's high transmissions. At $V_g = -4$ V, the modulation depth of the device is high as 0.1 dB/μm. The asymmetric voltage-dependent transmissions result from natural doping of the graphene by the substrate. Also, ideally, there should be a sharp transmission variation at $E_F = h\nu_0/2$. However, due to the defect and phonon perturbations in graphene, the transition process of on and off state are gradual.

Since graphene has a linear dispersion electronic structure around the Dirac point, this electro-absorptive modulator could be realized over a broad spectral range. Because graphene's Pauli-blocking of optical transition depends on the relative values between

the Fermi level and photon energies, the voltage thresholds for modulating light waves at different wavelengths are varied. Figure 6(e) displays the electrically modulated transmission over a wavelength range from 1350 to 1600 nm. The dashed line shows the trace for maximum transmission change rate with a quadratic function between the photon energies and drive voltage. It is governed by the relation between Fermi level and drive voltage, as the extracted data shown in Fig. 6(f).

Relying on graphene's high carrier mobility and large saturation velocity, this graphene-waveguide modulator is expected to have high-speed operation. Its dynamic response was estimated by applying a radio frequency electrical signal added on a static voltage. A fast-speed photodetector was employed to monitor the waveguide output. The 3 dB bandwidth of the devices at different drive voltages were estimated. The highest modulation speed was about 1.2 GHz with a high drive voltage due to the large detectable extinction ratio.[39] This limited bandwidth is not caused by the carrier transit time in graphene, but by the parasitic response of the device, which has a footprint of 25 μm^2.[98] Similar graphene-waveguide capacitor geometry was employed by Thourhout *et al.* to fabricate a broadband and athermal modulator operating at a speed of 10 GHz,[99] as shown in Figs. 6(g)–6(h). Recently, several graphene-waveguide modulators were fabricated on a compact chip using the CMOS processing line. Wide open eye diagrams with the dynamic modulation depth of 2.5 dB and low jitter were obtained at 6 and up to 10 Gb/s at the working wavelength of 1560 nm. This result constructively proved the possibility of graphene modulators for signal processing. The reduction of the dimension of the graphene capacitor is required to improve the operation speed. However, the modulation efficiency of the graphene-waveguide will be sacrificed as the result of the shortened light-graphene coupling length. In regard to this trade-off, Liu *et al.* proposed a double-layer graphene optical modulator by integrating the silicon waveguide with a capacitor consisting of two graphene layers, as schematically shown in Fig. 6(g). The waveguide's evanescent field couples with two graphene layers, which would improve the transmission attenuation over the same device length. Indeed, a modulation depth of 0.16 dB/μm was obtained at a moderate drive voltage of 5 V.[100] Another benefits of the dual-graphene structure is the simplified process of electrical contact with the absence of selective ion implantation on silicon. With the optimization of this structure, the low graphene contact resistance and small capacitor dimension allow the high-speed modulation. A device with a bandwidth of 35 GHz was reported by the same group.[101]

As discussed above, optical waveguides enhance graphene's optical absorption via its extended length, which unfortunately hinders the fabrication of high-speed modulators due to the large footprint. An alternative photonic structure to enhance light-graphene coupling is optical cavities. Different from waveguides, optical cavities recirculate light wave in a confined mode for an extended time, which, therefore, maintains strong light–graphene interactions in a compact structure. Photonic crystal (PC) cavity is one of the optical resonators with the highest Q/V_{mode}. Here, Q and V_{mode} are the quality factor and mode volume of the resonant modes in the PC cavity. The strength of the optical fields in the resonant mode is proportional to the factor of Q/V_{mode}. The PC cavity could provide high density of the electrical field to enhance light–matter interactions for the low-threshold micro-laser, bright single-photon source, and ultrasensitive microsensor.[102–104] The PC cavity fabricated in a subwavelength thick slab could provide a remarkable evanescent field to couple with 2D materials considering their atomic layer thickness. Its planar structure is compatible with the integration of 2D materials without quality degradation, as well as the construction of electrical devices. Strongly enhanced absorption, Raman, PL, and nonlinear processes of 2D materials have been realized with PC cavities.[86,87,105–107]

Gan *et al.* reported the monolayer graphene renders the reflection of a PC cavity to be nearly opacity, about 20 dB attenuation,[105] which indicates the implementation of optical modulators with high modulation depth by suppressing graphene's absorption electrically. As shown in Fig. 7(a), by integrating a silicon PC cavity with a graphene field effect transistor, a high-contrast electro-absorptive modulator was proposed.[108] To effectively tune graphene's Fermi level, an electrolyte layer was employed as the top gate. By forming two interface capacitors, over the graphene layer, an extremely strong vertical electric field is constructed, which could trap high carrier density. In the fabricated device, a PC cavity with a slotted defect was exploited, providing more optical field to couple with the coated graphene layer. Drain and source electrodes were deposited on the graphene layer, and the gate electrode was about 15 μm away from them, as shown in the optical microscopic image displayed in Fig. 7(b). An electrolyte layer (PEO plus $LiClO_4$) was spin-coated on the entire wafer. After the whole fabrication, the Q factors of the three resonant modes of the PC cavity decrease from (860, 2350, 3420) to (335, 610, 41,0) respectively, due to graphene's absorption,[108] which also reduced modes' reflection intensities. By applying varied V_gs, the graphene-PC cavity's reflection spectra were acquired, as shown in Fig. 7(c). From 0 to −7 V, graphene's Fermi level was tuned gradually to 0.8 eV, which is close to the photon energies of the resonant modes around 1550 nm. The three resonant peaks of the cavity reflection spectrum become strong and separate from each other due to the increased Q factors, which are enabled by the Pauli-blocked optical absorption in graphene. The voltage-dependent red- and blue-shifted resonant wavelengths were observed as well due to the variation of graphene's refractive index. Note, while the Fermi level is much higher than 0.4 eV (half photon energy of the incident light), the intensities and Q factors of the resonant peaks cannot completely recover to values of the original cavity. This might be attributed to the presence of residual absorption caused by intraband transition and defects in graphene. By changing V_g reversely, the strong resonant peaks lower and merge together, illustrating the electrically controlled modulations. With the voltage changed from 0 to 6 V, similar variations of the resonant peaks were obtained as those with negative drive voltages. By comparing the reflection intensities at the resonant wavelength at different V_gs, a modulation depth of 10 dB was achieved, which satisfies the requirement of signal processing. Because of the small capacitance of such a graphene-PC cavity, low power consumption was also anticipated. For the current device, the switching energy is about 340 fJ from a calculation of the capacitive charging energy. Also, the moderately broad linewidth of the resonant peak could promise better temperature tolerance than those devices with high Q resonators.

The response speed of electrolyte-gated modulator is restricted by the low mobility of ions in the electrolyte. Gao *et al.* couples a PC cavity with a dual-graphene capacitor to improve the operation speed,[109] as schematically shown in Fig. 7(d). A PC cavity was precisely placed on the BN-graphene-BN-graphene-BN heterostructure (graphene capacitor) to realize the coupling between cavity modes and the graphene–capacitor. Figure 7(e) displays the static electrical tuning

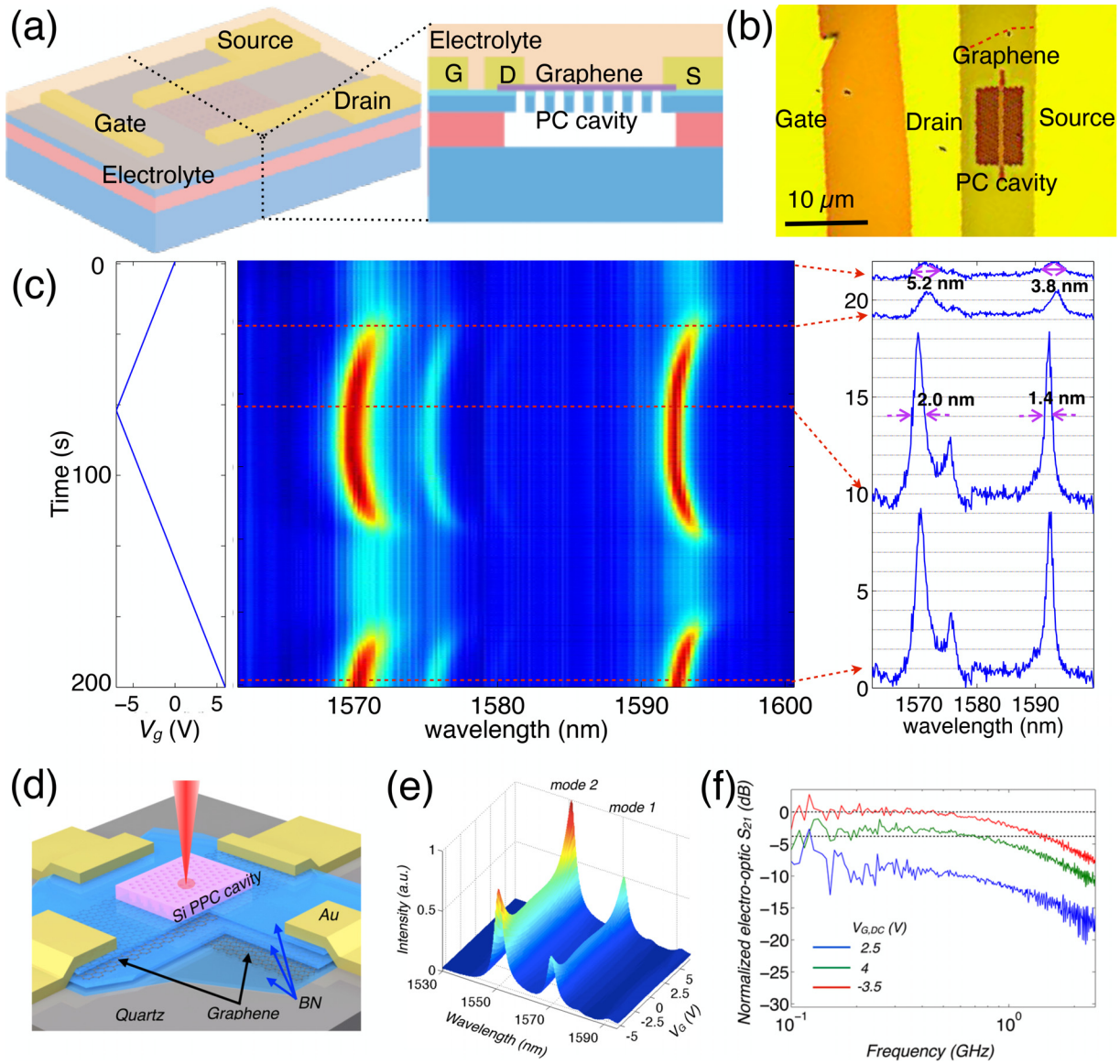

FIG. 7. High-contrast graphene electro-absorptive modulator integrated on a PC cavity. (a) Schematic illustration of an electrolyte gated graphene modulator integrated on a silicon PC cavity. (b) Optical microscopic image of the graphene-PC cavity modulator. (c) Reflection spectra of the PC cavity modulated by the top graphene layer at different V_g values, showing variations of the peak intensity and linewidth. (d) Schematic illustration of a modulator with a dual-graphene capacitor coupled with a PC cavity. (e) Static measurement of the reflection spectra from the device in (d) at different V_g values. (f) Dynamic responses of the electrical modulation from the device in (d). (a)–(c) Reproduced with permission from Gan *et al.*, Nano Lett. **13**, 691 (2013). Copyright 2013 American Chemical Society. (d)–(f) Reproduced with permission from Gao *et al.*, Nano Lett. 15, 2001 (2015). Copyright 2015 American Chemical Society.

result. By applying voltages on the graphene–capacitor, the resonant peaks of the PC cavity were modulated successfully with clear variations of intensity and linewidth. To evaluate the dynamic response, a radio frequency network analyzer was used to apply a high-speed electrical signal on the device. The intensity modulation of a resonant peak was monitored, presenting 3 dB attenuation at the frequency of 1.2 GHz [Fig. 7(f)]. The cutoff frequency is limited by the *RC* time constant of the dual-layer graphene capacitor, as deduced by the impedance measurement of the device. The graphene capacitor has an area of 100 μm^2 and a capacitance of 320 fF. The switching energy is approximately 1 pJ/bit. For the PC cavity, the overlap between the resonant mode and the graphene capacitor could be smaller than 0.5 μ^2. It is possible to reduce the dual-graphene capacitor to a size matching with the cavity area to lower the capacitance by approximately 200 times. This optimization could decrease the switching energy to 5 fJ/bit and increase the 3 dB cutoff frequency to 70 GHz.

Another widely employed on-chip optical resonator is a microring, which has advantages in ease of design, compact footprint, and

large fabrication tolerance. For real optoelectronic chips, microrings coupled with a channel waveguide have functioned as filters, modulators, and isolators. Graphene modulators constructed on microrings have more potentials for real device applications. A number of microring-based graphene modulators have been reported with capacitor structures consisting of dual-graphene layers or hybrid graphene–silicon.[110–112] There are resonant dips in the transmission of the waveguide side-coupled with the microring, whose extinction ratio is determined by the relative rates of the microring's mode loss and waveguide-coupling loss. Ideally, the extinction ratio could be 100% with the critical coupling condition when the microring's mode loss equals to the waveguide-coupling loss. If a graphene layer is covered on the microring, its absorption will induce more microring's mode loss, breaking the critical coupling condition. Hence, the integrated graphene not only reduces the Q factors but also decreases the extinction ratios of the resonant dips. Under this condition, the intensity of waveguide-transmission at the resonant dip increases. By electrically gating graphene to suppress the absorption, the critical coupling condition is recovered and the transmission intensity lowers, as schematically shown in Fig. 8(a). Phare *et al.* fabricated a dual-graphene capacitor on a silicon nitride microring [Figs. 8(b) and 8(c)]. Because of graphene's absorption, the resonant dip has a low Q factor (~800) and small extinction ratio (~8 dB) at $V_g = 0$ V. By gradually increasing V_g, the resonant dip red-shifts first and then blue-shifts with the continuously narrowed linewidths. The resonant dips shown in Fig. 8(d) indicate a modulation with a high depth could be obtained for a narrowband incident light considering the combined effects of wavelength shift and critical coupling. A voltage variation from −30 to −40 V would give rise to a depth of 15 dB. The requirement of high V_g originated from the thick dielectric layer between the two graphene layers, which actually generates a small capacitance for supporting a high-speed operation. The 3 dB bandwidth of the dynamic response was evaluated as 30 GHz [Fig. 8(e)], which also promises a clear eye diagram in the real data stream testing (the inset). The power consumption for per bit is estimated as 800 fJ, which is less than those reported in silicon-based modulators. Those pretty figure of merits make this modulator configuration has great potentials for future on-chip signal processing.

B. On-chip graphene electro-refractive modulators

As discussed above, graphene electro-absorptive modulators were realized via the suppressions of graphene's absorption due to the Pauli blocking. According to the Kramers–Kronig relation, the abrupt variation of optical absorption is accompanied by a large change in the refractive index. Hence, a graphene-based electro-refractive modulator is also expected by electrically tuning its carrier density for a moderately large variation of its refractive index. Actually, in Refs. 108 and 110, while the authors focused on amplitude modulations caused by the absorption-suppression, graphene's refractive index was tuned successfully, which had also induced considerable effects. For instance, as shown in Figs. 7(c) and 8(d), when a resonant mode of a microcavity couples with an electrically actuated graphene capacitor, the resonant wavelength red-shifts first and then blue-shifts as graphene's Fermi level is tuned away from the Dirac point gradually. According to the perturbation theory of electromagnetic wave, the shifts of cavity's resonant wavelength are attributed to the variation of graphene's refractive

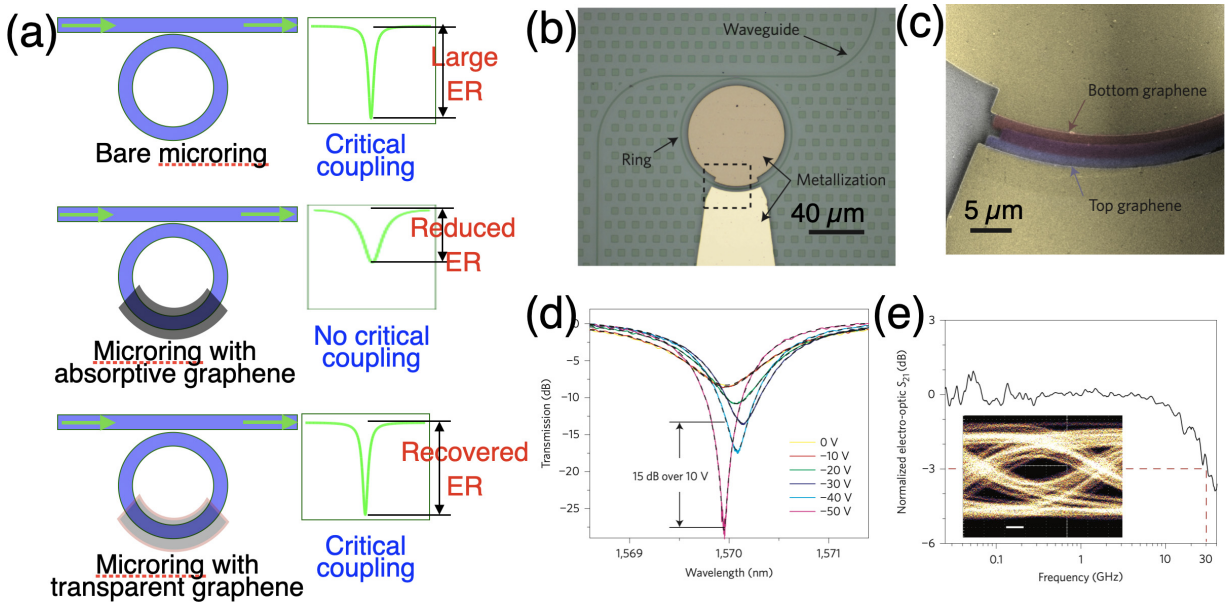

FIG. 8. Ultrafast graphene modulator integrated on a microring. (a) Schematic illustration of the graphene-modulated transmission from a microring side-coupled with a bus-waveguide, which is determined by the critical coupling related to graphene's absorption. ER: extinction ratio. (b) Optical microscopic image of the microring based graphene modulator. (c) SEM image of the device with the dual graphene layers covering over the microring. (d) Transmission spectra of the microring side-coupled with the bus waveguide at different V_g values, indicating large modulation depth. (e) Dynamic response of the modulator with a 3 dB bandwidth of 30 GHz. Inset shows the open 22 Gbps 27^{-1} pseudo-random binary sequence non-return-to-zero eye diagram. Reproduced with permission from Phare *et al.*, Nat. Photonics **9**, 511 (2015). Copyright 2015 Nature Publishing Group.

index.[108] For the result presented in Ref. 108, a resonant wavelength blue-shifted by 1.5 nm was obtained when the graphene field effect transistor was gated with a voltage of –7 V. Considering that the resonant peak has a linewidth of ~1.8 nm, this electrically actuated wavelength shift already enabled an electro-refractive modulator.

For the semimetal graphene, its complex refractive index (n_g) is governed by its complex optical sheet conductivity (σ_g) in the form of

$$n_g = \sqrt{1 + \frac{i\sigma_g}{\omega d_g \varepsilon_0}}, \tag{1}$$

where ω is the operating wavelength, $d_g = 0.34$ nm is the thickness of graphene, and ε_0 is the permittivity of free space. With an electrostatic doping of graphene, its complex conductivity controlled by E_F could be estimated by a simple theoretical model based on both inter- and intraband transitions,[113]

$$\sigma_g = \sigma_0 \Theta(\hbar\omega - 2E_F) + i\sigma_0[(4E_F)/(\pi\hbar\omega) - 1/\pi \ln|(2E_F + \hbar\omega)/(2E_F - \hbar\omega)|] \tag{2}$$

with $\sigma_0 = e^2/(4)\hbar$. This model neglects finite temperature and finite dephasing rates. In Ref. 108, doping-dependent complex conductivity of graphene for the wavelength around 1550 nm was extracted by referring to the Q factors and resonant wavelengths of the graphene-modulated resonant mode, as shown in Fig. 9(a). Equation (2) was

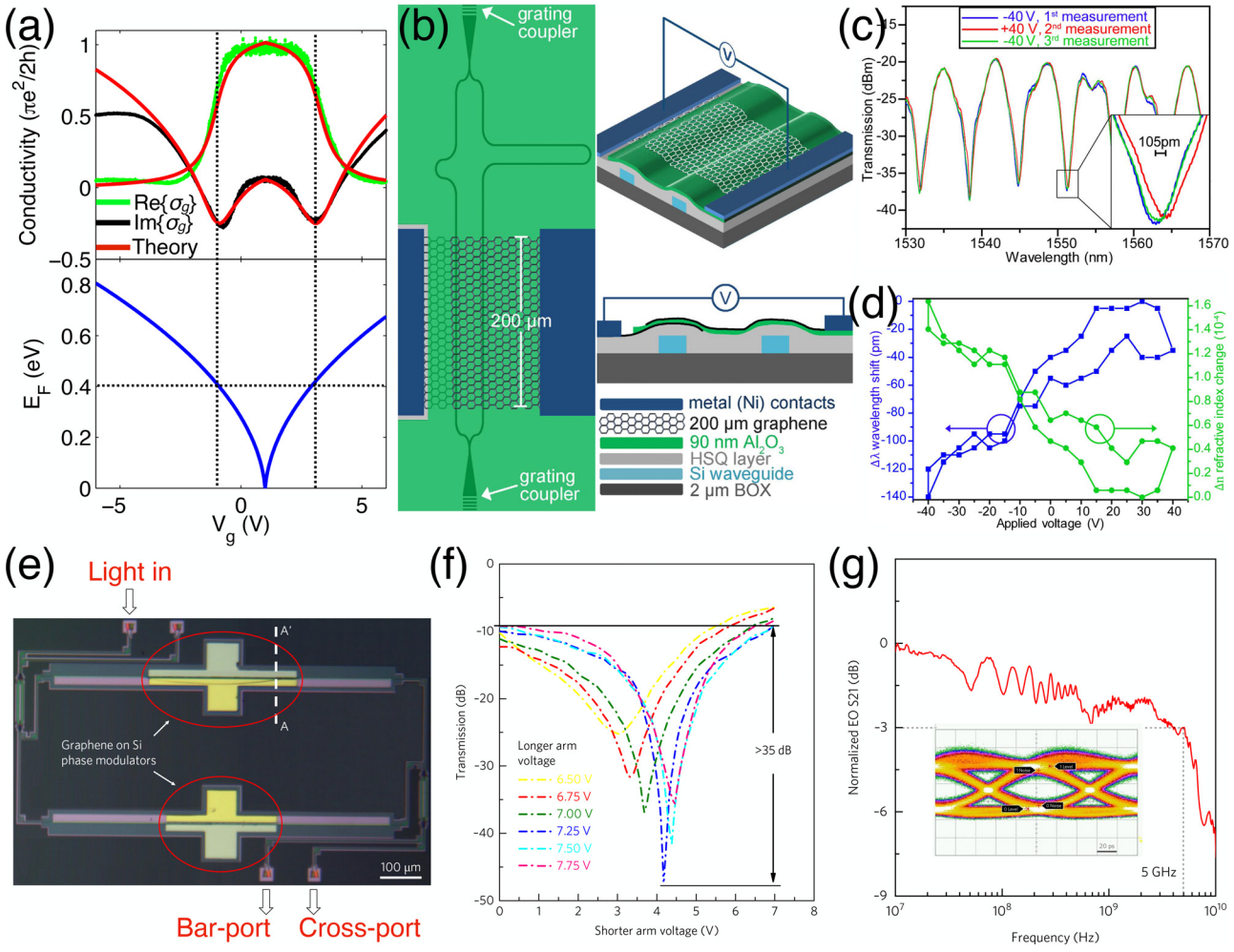

FIG. 9. Graphene electro-refractive modulators integrated on waveguides. (a) Complex conductivity of graphene for the wavelength around 1550 nm at different doping levels.[108] (b) Device structure of a graphene-integrated MZI for experimental verification of electro-refractive phase modulation in graphene. (c) Transmission spectra of the device in (b) at different drive voltage, showing the repeatability and spectrum shift. (d) Wavelength shift and the extracted refractive index variations from the device in (b) applied with varied voltages. (e) Optical microscopic image of a MZI modulator with graphene-silicon hybrid capacitors on both arms. (f) Transmissions of a 1550 nm laser at the bar port as functions of the shorter arm voltages when the longer arm voltage is fixed at different values. (g) Dynamic characterization of the MZI modulator in (e) showing 5 GHz bandwidth at 3 dB and an open eye diagram at 10 Gb/s. (a) Reproduced with permission from Gan *et al.*, Nano Lett. **13**, 691 (2013). Copyright 2013 American Chemical Society. (b)–(d) Reproduced with permission from Mohsin *et al.*, Sci. Rep. **5**, 10967 (2015); licensed under a Creative Commons Attribution (CC BY) license. (e)–(g) Reproduced with permission from Sorianello *et al.*, Nat. Photonics **12**, 40 (2018). Copyright 2018 Nature Publishing Group.

employed to predict these results with good agreement. When E_F increases to values larger than 0.4 eV (half photon energy of the incident light), the real part of the complex conductivity ($\mathrm{Re}\sigma_g$) approaches to zero gradually, giving rise to the neglectable optical absorption. The imagery part of the complex conductivity ($\mathrm{Im}\sigma_g$), corresponding to the real part of the refractive index, presents an inflection point with E_F close to 0.4 eV and has a larger dispersion for the even higher doping level. This is very promising to implement a graphene-based electro-refractive modulator with E_F tuned larger than 0.4 eV. The intrinsic absorption in graphene is forbidden effectively to guarantee the low insertion loss, and the refractive index changes greatly for the considerable phase shift. For example, calculated from Eqs. (1) and (2), a variation of refractive index larger than 5 is possible if the E_F is tuned from 0.4 to 1 eV.[114,115]

The graphene electro-refractive modulator was verified specially by integrating an electrically gated graphene layer on a silicon waveguide based Mach–Zehnder interferometer (MZI).[116] Since the variation of graphene's refractive index only results in a phase shift of the hybrid graphene-waveguide, the MZI would convert the phase change into an amplitude modulation. The device structure is schematically shown in Fig. 9(b). On one of the MZI arms, a capacitor formed by dual-graphene layers was built. Due to the strong optical absorption in graphene, the hybrid graphene-waveguide has a large attenuation of the transmission.[86] To maintain the extinction ratio of the MZI, the other arm of the MZI was covered by a graphene layer as well. Figure 9(c) displays the monitored transmission spectra when the dual-graphene capacitor was biased at 40 and −40 V. A clear shift of the minimum transmission was observed at the two voltages. The inset indicates the repeatability of the electro-optic modulating effect. When the voltage between the two graphene layers was applied between −40 and 40 V, the whole interference spectrum was shifted by 0.14 nm, corresponding to an effective refractive index change of 1.6×10^{-4}, as displayed in Fig. 9(d). Graphene's intrinsic absorption over the two arms was suppressed as well by the large electrical gating. Unfortunately, the employed structure had a thick spacer layer (90 nm) between the graphene capacitor and the silicon waveguide. The modifications of graphene's refractive index generate very weak effect over the effective refractive index of the hybrid graphene-silicon waveguide, which makes the device operation to require a high drive voltage. Also, since the graphene layer covered over another arm was not electrically gated, its intrinsic attenuation causes a large insertion loss of the device.

Sorianello *et al.* proposed a graphene electro-refractive modulator integrated on a silicon chip, showing figure of merits satisfying the requirement of real data processing.[117] As shown in Fig. 9(e), an MZI fabricated on a standard silicon photonic platform was integrated by an individual graphene capacitor on each arm. Here, two graphene capacitors were constructed by the doped silicon waveguide and the top graphene layer, which were separated by a 10 nm thick silicon oxide. This thin dielectric layer reduces the electrical voltage required to dope the graphene effectively. On the two arms, the graphene capacitors were designed with different lengths to facilitate the electrical tuning of their phase differences. To operate the device, both graphene capacitors were applied with static voltages close to 5 V to eliminate graphene's absorption. This could guarantee the low insertion loss of the whole device. Figure 9(f) shows static measurements of the electro-refractive modulator. With an input of 1550 nm laser, the bar port of the MZI was monitored with the varied gating voltages over the two graphene capacitors. By fixing the voltage applied on the longer arm, the device transmission was plotted as a function of the voltages applied on the shorter arm. For the minimum transmission points, the phase difference between the two arms approaches π. For instance, by applying 4.1 V to the shorter arm and 7.25 V to the longer one, the phase difference between the two arms approaches π. The modulation depth is maximized in this case, which is larger than 35 dB. This $V_\pi = 7.25$ V on the 400 μm long graphene capacitor corresponds to $V_\pi L = 0.28$ V cm, which is a fivefold improvement compared with state-of-the-art p-n junction-based silicon MZI modulators. The dynamic response of this electro-optic modulator was characterized using an electrical vector network analyzer. The S_{21} parameter of the network analyzer presented a 3 dB roll-off frequency to 5 GHz. As discussed by the authors, the bandwidth was mainly limited by the *RC* time constant originating from the silicon-graphene capacitor and series resistances. For the real data stream processing, a non-return-to-zero eye diagram was implemented, as shown in Fig. 9(g), which presented an open eye diagram at 10 Gb s^{-1} with a 4 dB modulation depth and a 6 dB signal-to-noise ratio. Calculated from the energy consumption of the charging and decharging capacitor, a value of 1 pJ per bit was obtained. While the reported device has disadvantages in operation speed and energy consumption compared to the pure silicon modulators[118] or III–V on silicon modulators,[119] graphene's decent electrical and optical properties endow great potentials to improve the performances of the proposed electro-refractive modulators. For instance, with a better graphene-preparing technique to improve the material quality and the metal contact, the series resistance from the graphene channel could be reduced by more than one order of magnitude. Furthermore, the two electrodes of the graphene-silicon capacitor could be designed in a traveling wave form to decrease the parasitic capacitance. The RF bandwidth could be greatly improved to a value around 50 GHz.[110] By replacing the graphene-silicon capacitor with a graphene-graphene capacitor over the silicon waveguide, the modulation efficiency could be doubled with the halved energy consumption.

C. On-chip graphene thermal modulators

In silicon photonics, high-speed (>GHz) modulators fabricated in silicon or III–V compound materials have very complicated and high-cost fabrication processes.[118,119] Contrastively, chip-integrated thermal modulators have virtues of ease-of-fabrication, high-efficiency, and broad optical bandwidth. Unfortunately, to heat the photonic structures for realizing refractive index variation, metal electrodes are required to align across the photonic structures. To avoid optical absorption by the metal heater, a thick silicon oxide layer (normally larger than 1.5 μm) would be deposited. However, such a thick upper-cladding layer will introduce low response speed and low heating efficiency due to its poor heat conductivity. In addition, the temperature in the metal heater is much higher than that in the photonic structures. Consequently, the temperature dynamics of the photonic structure is limited. While careful photonic designs to shrink the footprint or suspend the device could improve the efficiency and response speed to some extent, they inevitably introduce complex fabrication and operation.

Graphene has been well recognized as a conductive layer with high transparency. Its long-wavelength phonon transportation promises the high intrinsic thermal conductivity at room temperature,

which has been employed as spreaders in electronic and photonic devices.[120] With the combination of these attributes, it is possible to directly contact a graphene heater onto a photonic structure without the spacing layer by considering its moderate transparency. Compared with traditional thermal modulators with thick oxide layers, heat generated on the graphene layer could transfer to the photonic structure with fast speed and high efficiency. The fabrication of a graphene heater on the photonic structure is feasible considering its semimetal property and mature growth and transfer techniques. Its ultrahigh thermal conductivity facilitates fast transfer of thermal energy to the photonic structure, which also works as a fast thermal dissipation channel. Several graphene-based silicon modulators have been reported with response times smaller than 1 μs.[121,122] Heated by the top graphene heater, photonic structures have phase shifts due to the variation of refractive index. To convert it into intensity modulation, MZIs or resonators are essential, as shown in Fig. 10. Yu *et al.* covered the two arms of a silicon MZI with graphene layers to maintain the high extinction ratio, and one of the graphene layer was electrically heated to change the waveguide's refractive index, as shown in the left column of Fig. 10(a).[123] The middle column of Fig. 10(a) displays the transmission spectra of the MZI by applying an electrical voltage over the graphene heater. With the varied electrical powers from 0 to 110 mW, the interfering spectral fringe has a red shift of 7 nm. The high power consumption was the result of the large device footprint, which also gives rise to a long response time of about 20 μs [right column of Fig. 10(a)].

To improve the modulation efficiency and speed significantly, one of the possible routes is shrinking the device size. For example, Xu *et al.* employed a PC nanobeam cavity to couple with a graphene heater [Fig. 10(b)].[124] With the confinement of the total internal reflection of the silicon strip with the high refractive index and photonic bandgap of periodic air-holes, the nanobeam cavity has ultrasmall mode distribution (in a wavelength scale). It is possible to shape the graphene heater with a width in the scale of wavelength, promising the effective interaction with the heat field and optical field. As shown in the middle column of Fig. 10(b), a tuning efficiency of the resonant peak exceeding 1.5 nm/mW was realized. It could be considered as the record high value in graphene-assisted thermal-optic modulators. Also, the ultracompact structure of nanobeam-graphene allows the fast heat conduction for operating at a high speed modulation. The measured rising and falling times of the thermal-optic modulations are 1.11 and 1.47 μs, respectively. Microring or microdisk resonators were integrated with graphene heaters as well for thermal modulators,[121,125] while the efficiency is lower due to the larger mode volume. Different from resonators, slow-light waveguides have advantages of the enhanced light–matter interaction over a broadband wavelength range while the device footprint is compact.

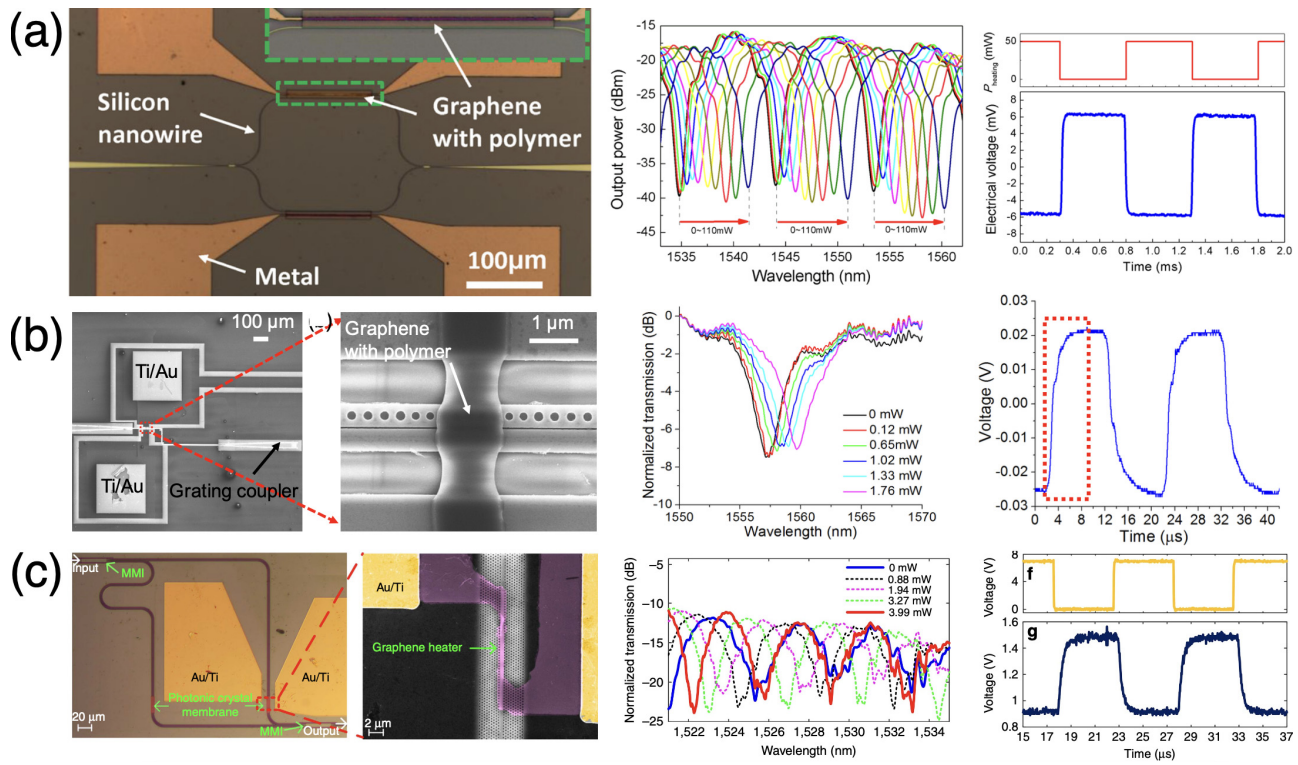

FIG. 10. Thermal-optic modulators assisted by graphene heaters, which are integrated on (a) MZI, (b) nanobeam cavity, and (c) slow-light waveguide. From left to right columns show the device images, spectra shifts with different thermal powers, and temporal response times, respectively. (a) Reproduced from Yu *et al.*, Appl. Phys. Lett. **105**, 251104 (2014), with the permission of AIP Publishing. (b) Reproduced with permission from Xu *et al.*, Opt. Express **25**, 19479 (2017). Copyright 2017 Optical Society of America. (c) Reproduced with permission from Yan *et al.*, Nat. Commun. **8**, 14411 (2017). Copyright 2017 Author(s); licensed under a Creative Commons Attribution (CC BY) license.

As mentioned above, the intrinsically slow processes of heat accumulation and dissipation still limit the dynamic speed of these thermal-optic modulators. The graphene thermal modulator with the highest speed was reported by Yan *et al.*,[122] as shown in Fig. 10(c). This device employed a PC slow-light waveguide to integrate with a graphene strip heater. Owing to the enhanced light–matter interaction by the slow-light, it is possible to reduce the device footprint as well for improving the tuning efficiency and speed. In addition, the graphene channel is etched into a strip line overlapping on the waveguide, which guarantees the effective employment of heat to control the light propagation. To accelerate the heat conduction further, the buried oxide layer beneath the silicon PC waveguide was etched. The characterization results showed a high tuning efficiency of 1.07 nm/mW over the whole telecom-band and a fast temporal response with a rising (falling) time of 750 (525) ns.

D. Graphene-enabled fiber-based modulators

Optical fibers have revolutionized the applications of light in communication, signal processing, and sensing. Unfortunately, silica's intrinsic passive attributes cannot support the realizations of fiber-based modulators, switches, phase shifters, etc. External active devices have to be connected to the fiber lines for functional optical systems. Recently, graphene's unique electrical and optical properties have attracted researchers to make fiber-based modulators, which have potentials to simplify the package of optical systems. To couple graphene with the optical field in optical fibers, microfibers with diameters of 1–10 μm were fabricated by flame heating or acid etching, or "D"-shaped fibers were fabricated by polishing one-side of the conventional fibers. These fibers could provide leaky evanescent fields around them to couple with the integrated graphene layer. CVD-grown or exfoliated graphene layers were wrapped around the microfibers. Figure 11(a) displays optical microscopic images of CVD-grown graphene-wrapped microfibers, which were fabricated by flame heating and acid etching.[41,126] By simulating the guiding mode distributions of the graphene-microfiber, the graphene–light interaction could be estimated, as shown in Fig. 11(b).[41] The lower inset plots the zoomed location of the graphene layer, which indicates that the graphene layer induces an abrupt change in the optical field due to its large refractive index. Graphene's absorption causes propagation attenuations of 0.49and 1.84 dB/mm for the guiding modes at 980and 1540 nm, respectively. Hence, microfiber's diameter and graphene length should be designed carefully to avoid large insertion loss of the modulators.

Because of graphene's gapless Dirac-fermionic band structure, the absorption of microfiber's evanescent fields could convert into thermal energy with very high efficiency, which, therefore, heats the microfiber. Relying on the fiber's thermo-optic effect, a considerable refractive index variation could be obtained. Similar to the above on-chip thermal modulators, all-optical fiber modulators could be implemented. Gan *et al.* fabricated a device by wrapping a 5 mm long graphene around a microfiber with a diameter of 10 μm. A phase shift exceeding 21π with a nearly linear slope of 0.091 π/mW (0.192 π/mW) was obtained when pumped by light at the wavelength of 980 nm (1540 nm). It enables all-optical switching with a modulation depth of 20 dB and a rising (falling) time of 9.1 ms (3.2 ms)[41] [Fig. 11(c)]. With this graphene-assisted thermo-optic effect in the microfiber, a microfiber Bragg grating and a microfiber knotted ring were all-optically tuned successfully for carrying out optical bistability and switching with high extinction ratios.[126–128] These devices operate with the refractive index change of the whole microfiber, ensuring a high efficiency and low power consumption. As a consequence, featured with all-in-fiber, low power requirement, and ease of fabrication, these graphene-microfiber devices may open the door for graphene's realistic applications in all-optical signal processing.

An alternative approach to modulating the optical signal in the graphene-microfiber is tuning graphene's optical properties, such as absorption or refractive index. The graphene's linearly dispersed electronic structure around the Dirac point allows easy tuning of carrier density all-optically, which is in the timescale of picoseconds. By inputting ultrafast pulses with high energy into the graphene-microfiber, the optical field coupled with graphene could saturate its absorption via the Pauli blocking or change the refractive index via the Kerr effect. The experimental configuration for all-optical modulations is displayed in Fig. 11(d),[40,129] respectively. The saturable absorption in graphene requires a simple implementation, which could be realized by measuring direct transmission of the hybrid graphene-fiber. To utilize the graphene's Kerr effect, which is expected to introduce a change of the effective refractive index in the graphene-microfiber, an MZI is needed to convert the phase modulation into the amplitude variation. In both working mechanisms, modulation depths exceeding 40% were obtained, and the response times were around 2 ps relying on graphene's ultrafast carrier dynamics, as shown in Fig. 11(e). In these ultrafast all-optical modulators, to significantly promote the carrier density in graphene, effective graphene-light interaction is essential. Therefore, the microfiber's diameters were preferred to be around 1 μm for more evanescent field leaking out. At the same time, considering the scattering impurity and dephasing effect of carriers in graphene, even the saturable absorption is achieved at high pump energy, graphene's intrinsic absorption loss cannot be absolutely inhibited, i.e., it is still quite lossy in the graphene-microfiber. Hence, for the 1 μm thick microfiber, the graphene-coating length should not be very long, and the possible optimized range is about 10–40 μm.[40,129] Though ultrafast modulations were realized, this tiny thicknesses of the microfibers mount challenges for their realistic applications due to the fragile structure during the device fabrications and operations. In contrast, thermal-optic graphene-microfiber modulators release the requirement of very thin diameter attributed to the high efficiency of thermal-optic effect, which improve the device stability. The graphene-cladding length does not have critical demands either due to the low absorption by the graphene layer coated on a much thicker microfiber.[41,126–128]

It is also possible to electrically fabricate tuned graphene devices on fibers, as shown in Fig. 11(f). Lee *et al.* transferred a graphene layer onto a "D"-shaped fiber and made an electrolyte-gated graphene capacitor.[130] The fiber's planar surface provides a flat platform to deposit metal electrodes as well as leak guiding mode to couple with graphene, as indicated in Fig. 11(f). Since the leaking optical field from the "D"-shaped fiber is much weaker than those from a tapered microfiber, a long graphene layer is required to achieve a considerable interaction between the coated graphene and the propagating mode. As shown in Fig. 11(g), the fabricated device has a graphene length of ~5 mm. The electrical tuning mechanism of this devices is similar to the one reported in Ref. 108. The drop-cast ion liquid could provide an ultrathin (1 nm) carrier layer at its interface between graphene, generating a strong electric field to dope graphene into high Fermi levels.

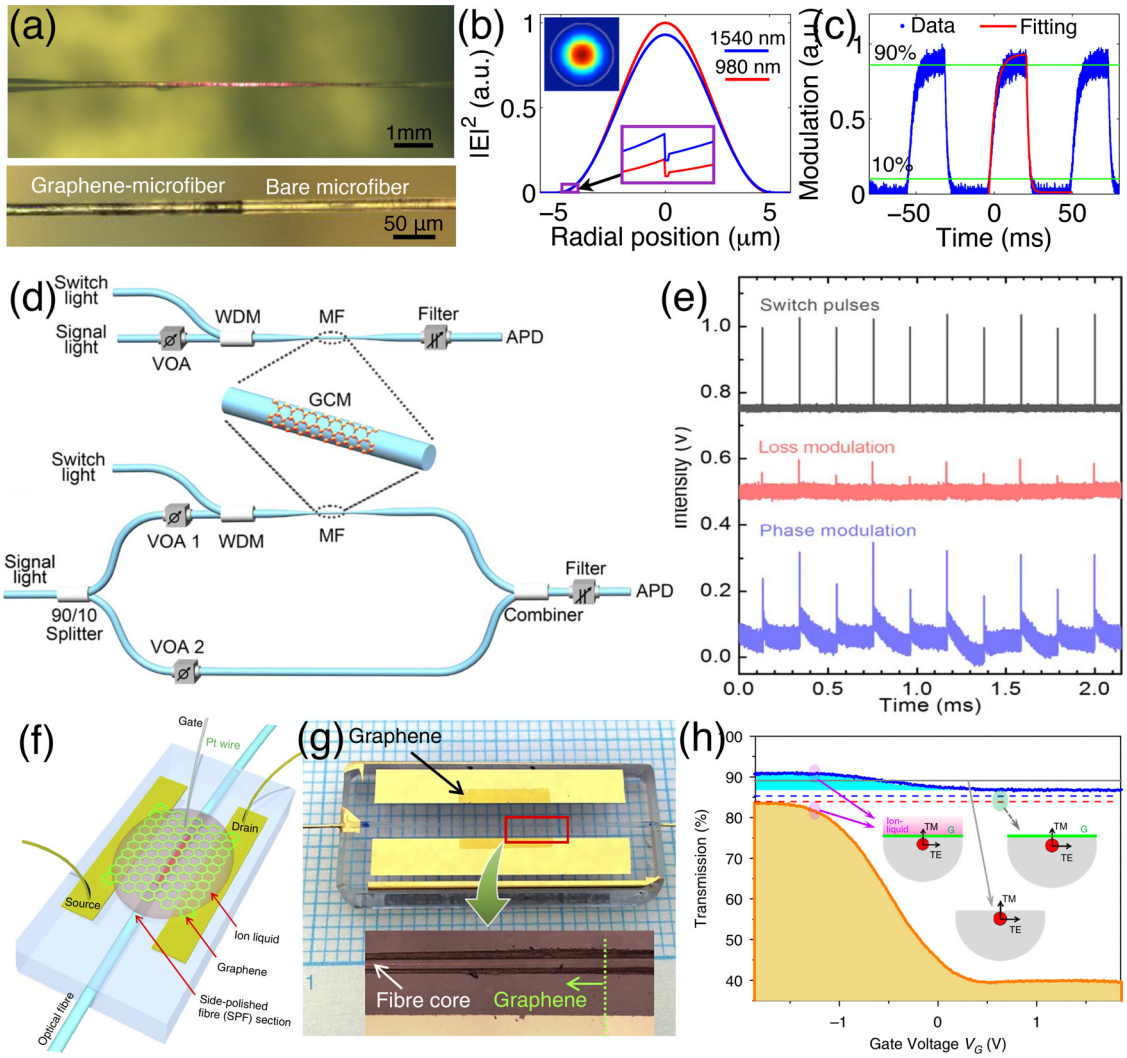

FIG. 11. Optical fiber-integrated graphene modulators. (a) Optical microscopic images of graphene-wrapped microfibers fabricated by flame heating (top) and acid etching (bottom). (b) Guiding modes across the center of the graphene-microfiber at the wavelengths of 980 and 1540 nm, where the upper inset is the 2D distribution of the mode at 1540 nm (graphene is indicated by the white line) and the lower inset is a zoomed-in image at the fiber edge. (c) All-optical modulation result obtained from the device in (a). (d) Two experimental architectures to realize ultrafast all-optical modulator utilizing saturable absorption (top) and Kerr effect (bottom) in the coated graphene layer. (e) Ultrafast modulation results from a graphene-coated microfiber operating in the regimes of loss modulation and phase modulation, respectively. (f) Schematic illustration of an electrolyte gated graphene-fiber device, where a "D"-shaped fiber was employed to provide a platform for constructing graphene field effect transistor. (g) Fabricated electrically tunable graphene-fiber device, showing a graphene length about 5 mm. (h) Tuned transmission from the graphene-coated fiber by applying different gate voltages. (a)–(c) Reproduced with permission from Gan *et al.*, Optica **2**, 468 (2015). Copyright 2015 Optical Society of America. (d)–(e) Reproduced with permission from Yu *et al.*, Optica **3**, 541 (2016). Copyright 2016 Optical Society of America. (f)–(h) Reproduced with permission from Hong *et al.*, Nat. Commun. **6**, 6851 (2015). Copyright 2015 Author(s); licensed under a Creative Commons Attribution (CC BY) license.

Figure 11(h) displays the gate-varied transmission of the fabricated device coated with the graphene monolayer. A modulation depth over 40% was obtained with a gate voltage of 2 V. Devices with even thicker graphene layers were fabricated and tested. A high modulation depth exceeding >90% was realized from a device with the graphene quad-layer. Considering the slow carrier mobility of the ion liquid (smaller than 100 Hz), the employment of this electro-optic modulator in fiber-based signal processing is limited. However, it can function as an active controller in an ultrafast laser considering its compatibility with all-fiber systems.[130]

IV. MID-INFRARED OPTICAL MODULATORS BASED ON GRAPHENE AND BLACK PHOSPHORUS

Mid-infrared electromagnetic waves in the wavelength range from 2 to 30 μm are of great utility for chemical bond spectroscopy, free-space communications, environment/health sensing, etc. Despite the

tremendous efforts in developing mid-infrared sources and detectors,[131] a viable strategy toward realizing high-performance mid-infrared modulators remains elusive. For instance, solid-state mid-infrared modulators based on semiconductor quantum wells require sophisticated material growth and cryogenic temperatures and the modulation depth is small.[132] Liquid crystal and digital micro-mirror based spatial light modulators suffer from limitations including slow response speed and complex instrumentation.[133]

The above discussed largely tunable optical conductivity in graphene in the telecom-band is valid for the mid-infrared radiations as well, which promises high-performance mid-infrared modulators on the basis of the easy fabrication of graphene and the simple implementation of electrical tuning. The limited interaction between the ultrathin graphene and the single-passed mid-infrared light should be overcome to realize a high modulation depth. The graphene modulators in the telecom-band could be implemented by integrating it on optical fibers, waveguides, or resonators to enhance light-graphene interactions. However, determined by the main application scope of mid-infrared modulators, they should be operated in the free-space configuration. Hence, plasmonic structures/antennas were widely employed to integrate graphene for enhancing mid-infrared light-graphene interactions.[134–137] In the hybrid graphene-plasmonic structures, the free-space mid-infrared illumination could be captured by the plasmonic antennas effectively. Furthermore, the localized hotspots in the plasmonic nanogaps could interact with the graphene strongly. On the other hand, the plasmonic antennas are normally designed with resonance modes in the mid-infrared range. By tuning the optical conductivity of graphene, the resonance modes of the hybrid graphene-plasmonic structures would be shifted in the wavelength or varied in the reflection/transmission amplitude, giving rise to the expected mid-infrared modulations. For example, Zeng *et al.* deposited arrays of "I"-shaped Au nanoantennas on a graphene field effect transistor, which has slightly conducting amphorous silicon as the back gate and 6 nm thick Al_2O_3 as the dielectric layer.[135] With the free-space illumination of a broadband mid-infrared light, the reflection spectrum of the hybrid graphene-plasmonic metasurface showed a clear resonance dip. By applying a low gate voltage around 7 V, a resonance wavelength shift of 1 μm was observed around the central wavelength of 8 μm, resulting in a large intensity modulation with a depth up to 90%. The low operation voltage benefits from the ultrathin dielectric layer. The modulation speed was examined as well, which could exceed 1 GHz. With the virtues of low-voltage operation and fast modulation speed, a prototype mid-infrared spatial light modulator was demonstrated to function as an electrically encoded aperture or mask, realizing single-pixel imaging with a high frame rate.

In addition to the hybrid graphene-plasmonic structure, graphene has intrinsic plasmonic responses in the mid-infrared range due to its intermediated carrier concentrations (10^{12}–10^{13} cm^{-2}). By patterning graphene into nanostructures to capture the free-space illuminated mid-infrared radiations, plasmonic resonance modes in graphene could be excited. If the optical conductivity of graphene was tuned electrically, the transmitted amplitude of the mid-infrared light through the graphene nanostructure could be modulated around the plasmonic resonance modes.[138] Unfortunately, because only the patterned graphene is the active layer of the modulator, the coupling efficiency with the free-space mid-infrared radiation is low, which results in a very small modulation depth about 6%. Also, limited by the large device dimension, the capacitance is too large to allow the fast modulation speed. Note that graphene is too lossy to exhibit strong plasmonic properties in the mid-infrared, especially at energies above the 200 meV optical phonon energy of graphene.[139] It would limit the performance and future development of mid-infrared modulators based on graphene plasmonics.

Though the plasmonic structures used to hybrid with graphene could be designed to realize modulators over the whole mid-infrared spectral range, the operation wavelengths of these reported graphene mid-infrared modulators were mainly in the wavelength range between 6 and 8 μm. For realizing modulators in even shorter mid-infrared wavelength range, layered black phosphorus (BP), another emerging 2D material, has much better optical and electronic properties. In addition, compared with the graphene based mid-infrared optical modulators leveraging the intraband transition, BP's on-resonance optical transition has stronger light-matter interactions, which is friendly for the higher modulation depth. The insertion loss could be got around with the assistance of the bandgap as well, as discussed in the following.

BP was first synthesized in 1914. Bulk BP was heavily investigated to reveal interesting physical properties, such as high carrier mobility and superconductivity.[140] Inspired by various exotic properties obtained from mono- and few-layer graphene and TMDCs, BP was mechanically exfoliated into atomically thin flakes to perform electrical and optical characterizations.[24,141–144] These rediscoveries of BP indicated its few-layer could well bridge the gap between graphene and TMDCs for constructing 2D material-based electrical and optoelectronic devices. For a field effect transistor, graphene promises ultrahigh carrier mobility while fails in the on/off current ratio due to the gapless. The large bandgaps of TMDCs could provide large on/off current ratios; unfortunately, the carrier mobilities meet obstacle to surpass silicon's performance. Few-layer BP has been demonstrated to support field effect transistors with drain current modulations on the order of 10^5 and carrier mobilities up to 1000 $cm^2V^{-1}s^{-1}$.[141] To respond an optical radiation, BP's direct bandgap facilitates strong light-matter interactions, and the value could be varied from 0.3 to 2 eV by changing the layer numbers.[145,146] These are different from graphene's zero-bandgap and large bandgap in TMDCs (normally larger than 1.5 eV). Also, TMDC experience a transition from direct to indirect bandgap when the layer number is increased from monolayer to few layer.[31] Varying BP flakes from tetralayer to bulk, the direct bandgaps change between a range of 0.6 and 0.3 eV, corresponding to the mid-infrared wavelength range of 2–4 μm.[146] Recent reliable results of electrical doping on few-layer BP encouraged the implementation of BP-based mid-infrared optical modulators.[24,141,142]

Lin *et al.* first theoretically investigated the electro-optic properties of few-layer BP flakes for optical modulations in the mid-infrared spectral range.[147] As widely demonstrated in graphene and TMDCs, an out-of-plane electric field could modify their electronic structures remarkably due to the strong vertical confinements of wave functions. Similarly, BP thin films could be considered as a quantum well, whose band edge allows a reliable electrical engineering to change the optical responses. As schematically shown in Fig. 12(a), an out-of-plane electric field is applied via a BP capacitor or field effect transistor to shift its band edge. Because of BP's semiconducting nature, it would have a screening length of the out-of-plane electric field on the order of 10 nm, which, thereby, allows the effective modification of band structure over the thin BP layer. Relying on the modified band structure,

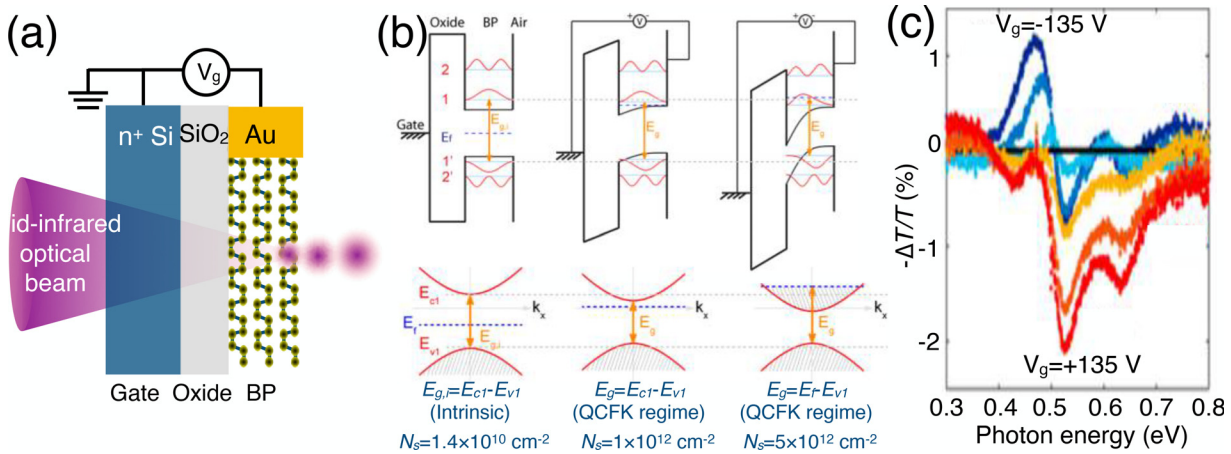

FIG. 12. Modulations of mid-infrared radiation using BP. (a) Schematic illustration of a BP-based mid-infrared modulator in a transmission regime. (b) Schematic of energy band diagrams and wave functions (top), and energy dispersion diagrams (bottom) of a 5 nm thick BP at different doping levels. (c) Modulations of transmission spectra from a BP field effect transistor with a 6.5 nm thick flake by comparing with the transmission spectrum at zero bias. (b) Reproduced with permission from Lin *et al.*, Nano Lett. **16**, 1683 (2016). Copyright 2016 American Chemical Society. (c) Reproduced with permission from Whitney *et al.*, Nano Lett. **17**, 78 (2017). Copyright 2017 American Chemical Society.

BP's optical conductivity (optical absorption) for a mid-infrared optical beam at a specific wavelength could be electrically controlled, giving rise to the transmission modulation of the BP flake.

Different from the gapless graphene, there are two effects attributed to the modifications of BP's optical conductivity in the mid-infrared range, which leverage the variations of band structures or carrier densities. Figure 12(b) schematically shows the energy band diagrams and wave functions (top), and energy dispersion diagrams (bottom) of a 5 nm thick BP with different carrier densities.[147] (1) For a BP flake without doping or doped lightly, its optical bandgap E_g is defined as the optical transition energy between the highest filled state in the valence band and the lowest unoccupied state in the conduction band. In the intrinsic state, its electron carrier density is estimated to be 1.4×10^{10} cm^{-2}. The intrinsic bandgap is $E_{g,i} = E_{c1} - E_{v1} = 0.62$ eV, where E_{c1} and E_{v1} are the energy levels of the first conduction and valence subbands, respectively, as indicated by the left column of Fig. 12(b). (2) With the application of an external electrical gate, because of the electric field screening across the BP quantum well, electronic bands in different layers have a relative bending [middle column of Fig. 12(b)]. It brings the electron and hole subbands closer, which subsequently reduce E_g. This bandgap shrinkage could be described by the quantum-confined Franz–Keldysh (QCFK) effect. It would make the BP film respond/absorb mid-infrared light with photon energies smaller than BP's intrinsic bandgap. (3) With an electrical voltage applied over the gate-oxide-BP layers, besides the effective electric field across the BP layer, carrier density is changed as well in the gate-oxide-BP parallel capacitor, corresponding to the shifted Fermi levels E_F. As V_g increases, the Fermi level could be raised (lowered) into the conduction (valence) band due to the increased carrier densities [right column of Fig. 12(b)], such as in the level of 5×10^{12} cm^{-2}. The strengthened degenerated carrier states make the optical transitions be Pauli blocked, i.e., the Burstein–Moss shift (BMS) effect. Different from the QCFK regime, the BMS regime broadens the optical bandgap E_g, which is defined as $E_g = E_F - E_{v1}$. This enables the modulation of the optical conductivity with larger photon energy than BP's intrinsic bandgap $E_{g,i}$. The absorption of photons with energy larger than $E_{g,i}$ is inhibited if V_g is larger enough to reach the BMS regime. Hence, by electrically gating BP for mid-infrared modulations, the two opposite electro-absorption mechanisms (QCFK and BMS effects) should be considered together. The prominent role of the two effects is determined by the doping level and operating wavelength.

Note that BP is an anisotropic material due to different effective masses along the armchair and zigzag crystalline axes. The above calculations were considered for the light polarized along the armchair direction, which has a higher optical conductivity and is more favorable in modulation applications. In addition, for BP films with varied thicknesses, the QCFK and BMS effects have different layer-dependences of the energy shifts. The BMS effect is only determined by the relative position between the Fermi level and conduction/valence band. Its energy shift is not sensitive to the BP thickness. However, since the electric field screening across the BP layer is the origin of band-bending, the energy shift induced by the QCFK effect for a thicker BP film has a larger value. For BP flakes thinner than the tetralayer, the optical transition bandgap is around the telecom-band.[148] The excitonic effect would contribute to the optical conductivity in this case. The band-bending of QCFK effect is very weak due to the thin layers. Fortunately, similar to the excitonic modulation of visible light in TMDC monolayers, an electric field could be applied to tune the oscillator strengths between excitons and trions to realize a promising modulation on the telecom-band light.

These theoretical predictions of BP's optical responses in mid-infrared spectral ranges were experimentally verified by different groups.[149,150] As shown in Fig. 12(c), transmission variations of the optical signals with photon energies in a range between 0.3 and 0.8 eV (i.e., the wavelength ranging from 1.55 to 4.1 μm) were extracted from a BP field effect transistor with a 6.5 nm thick BP flake. By comparing the transmission spectra obtained at different V_gs to that at zero bias, modulation depths around 2% were obtained. The oscillations of the

modulation amplitude and sign could be attributed to the co-contributions of the QCFK and BMS effects.[149] Similar results were reported in Ref. 150, which also experimentally studied the dependence of BP thicknesses and doping levels. While the reported modulation depths of the vertically illuminated BP capacitors cannot support the realistic applications yet, a configuration with the integration of an optical waveguide or cavity could be employed to increase the light–BP interaction and the modulation depth.[86,147,149,151] Finally, it is worth noting that these proposed and realized modulators employ the shift of BP's absorption band edge to control optical amplitude directly. A phase-modulation should also exist in few-layer BP because the absorption variation is accompanied by the modified refractive index according to the Kramers–Kronig relation.

V. TERAHERTZ MODULATORS BASED ON 2D MATERIALS

A terahertz electromagnetic wave, lying between radio frequency and infrared spectral bands, is attracting research interest due to its important applications in biochemical sensing, communication, non-destructive imaging, etc. Similar to the active devices in the mid-infrared range, while terahertz sources and detectors received rapid progress recently, the modulations of terahertz waves still lack efficient devices. The performances, including modulation depth, broadband operation, insertion loss, and on-chip integrability, are required to be improved. A variety of terahertz electro-optic modulators are developed based on semiconductor heterostructures containing a 2D electron gas, where electrons can be accumulated or depleted by an applied voltage. However, limited by the electronic properties of the conventional semiconductor heterostructure, it is difficult to achieve a tunability of electron density larger than 1×10^{12} cm^{-2}. Hence, these devices can only modulate the terahertz wave with a low depth, which are normally in a range of a few percent. Even with the combinations of metamaterials or plasmonic structures,[152] the modulation depths are still no more than 30%, which sacrifice their broadband operations though. Contrastively, the graphene's carrier concentration could be electrically tuned to a level as high as 1×10^{14} cm^{-2}, which also has outstanding carrier mobilities. In addition, these carrier attributes are available for both holes and electrons owing to graphene's symmetric conical band structure. These give rise to reasonably tunable conductivity ranges relative to both electrons and holes for modulating terahertz waves, which perform better than conventional semiconductor heterostructures realized only by electrons.

Xing *et al.* first theoretically proposed the graphene-based terahertz modulator after a comprehensive analysis of limits of the 2D electron gas based terahertz modulator.[153] Graphene was considered as a "tunable metal," which could function as the gate electrode to bias the 2D electron gas in a conventional semiconductor with a low insertion loss. In the calculations, it was indicated that a graphene monolayer can be nearly transparent when its Fermi level was tuned at the Dirac point. In contrast, the absorption on the terahertz beam could be almost 100% when the Fermi level is tuned for maximum conductivity. This geometry supports broadband, polarization-independent, and chip-integratable terahertz modulators.[153]

The device structure of the first experimentally demonstrated graphene-based terahertz modulator is displayed in Fig. 13(a).[154] To tune graphene's carrier concentration, a *p*-type silicon substrate is chosen to provide a back gate, which is electrically separated from graphene with a thin layer of silicon oxide. By applying V_g between them, the graphene's Fermi level will be shifted and the conductivity varies correspondingly. The transmission of the terahertz wave was measured to estimate the modulation by the graphene layer. In the visible and infrared ranges, graphene couples with light via the interband transition of carriers, whereas, for terahertz range, it is dominated by intraband transitions. In this long wavelength range, graphene acts as a conductive film and the optical conductivity can be described by a simple Drude model. With this principle, on the fabricated devices, if there is no applied voltage, the graphene's Fermi level locates at the Dirac point, wherein introducing minimum insertion loss or signal attenuation. When an out-of-plane electric field is applied, graphene's carrier density was increased to shift the Fermi level and increase the optical conductivity, which could reduce the transmission of the terahertz wave. Figure 13(b) displays the measured static characteristic of graphene's electrical conductivity and transmission of the terahertz wave at 600 GHz. As expected, the transmittance increases with the decreased electrical conductivity of graphene. Over the range of 570–630 GHz, the measured transmittances showed a flat modulation depth of 16% between the applied voltages of $V_g = 0$ and 50 V, indicating its broadband operation. To evaluate the experiment results, simulations with the Drude model were implemented by considering graphene's DC conductivities at different V_gs, which show their excellent agreement. The dynamic characteristic of the fabricated graphene terahertz modulator was measured as well by modulating V_g with different speeds. The response waveform to a square modulation voltage indicates a rising time of 38 μs, and the measured 3 dB bandwidth is ~20 kHz. This modulation speed is mainly limited by the device's *RC* time constant, which has a large capacitance *C* due to the large active device area.

To further improve the modulation depth of graphene-based terahertz modulator, Xing *et al.* modified the structure displayed in Fig. 13(a).[155] A metal electrode was deposited on the backside of *p*-silicon, which functioned as the gate electrode and the reflector of terahertz wave. When an electrical gate was applied between metal electrode and graphene layer, carriers got accumulated over the graphene layer and the interface of silicon/silicon oxide. For *p*-silicon, the carrier concentration at the top layer will not result in the significant variation of the optical conductivity. The modulation of terahertz wave is mainly achieved by the graphene active layer, which has a strong shift of conductivity. The terahertz wave has a zero intensity at the back metal, and the wave strength in the graphene layer depends on the optical thickness of the substrate and the terahertz wavelength. If the total thickness of the silicon and silicon oxide layers is an odd-multiple of the terahertz wavelength, the field intensity in graphene is at maxima. In a fabricated device, a modulation depth of 64% was obtained at the operation frequency of 620 GHz, which is about four times higher than that obtained in the single-passed transmission geometry.[154] However, for the frequency of 590 GHz, there is no any change of the reflection with different applied voltages, which could be attributed to the overlap of graphene with the minimum strength of the terahertz wave. Hence, this graphene modulator based on reflection geometry can only work in a narrowband range considering the interference of the incident and reflected waves, while the modulation depth is significantly improved.

Another approach to boosting the modulation depth is integrating graphene into a metamaterial, as shown in Fig. 13(c).[156] An array

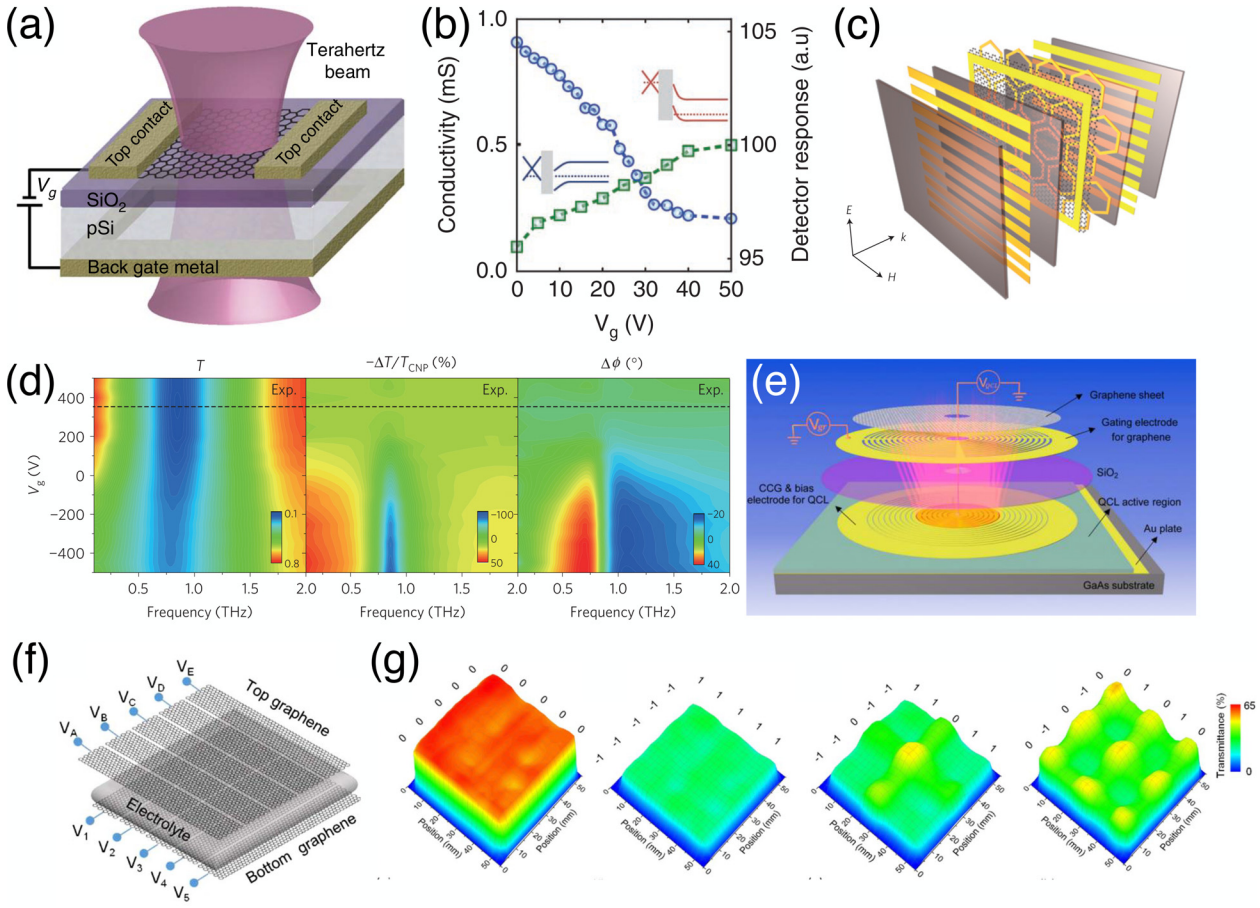

FIG. 13. Electro-optic terahertz modulator based on graphene. (a) Schematic illustration of a graphene-based terahertz modulator. (b) Measured graphene electrical conductivity and transmission of the terahertz wave at 600 GHz at different V_gs from a device with the geometry in (a). (c) Schematic representation of compositions of an active graphene metamaterial. (d) Measured transmission (T) of the terahertz wave through the graphene metamaterial at different V_gs values and the estimated changes of amplitude $[-\Delta T/T_{CNP}(\%)]$ and phase $[\Delta\phi(^\circ)]$. (e) Monolithically integrated graphene modulator on a terahertz quantum cascade laser. (f) Terahertz spatial light modulator enabled by dual layers of graphene ribbons, which sandwich an electrolyte layer. (g) Terahertz transmission images of the spatial light modulator in (f) with various voltage configurations recorded at a frequency of 0.37 THz. (a) and (b) Reproduced with permission from Sensale-Rodriguez *et al.*, Nat. Commun. **3**, 780 (2012). Copyright 2012 Author(s); licensed under a Creative Commons Attribution (CC BY) license. (c) and (d) Reproduced with permission from Lee *et al.*, Nat. Mater. **11**, 936 (2012). Copyright 2012 Nature Publishing Group. (e) Reproduced with permission from Liang *et al.*, ACS Photonics **2**, 1559 (2015). Copyright 2015 Author(s); licensed under a Creative Commons Attribution (CC BY) license. (f) and (g) Reproduced with permission from Kakenov *et al.*, Opt. Lett. **40**, 1984 (2015). Copyright 2015 Optical Society of America.

of meta-atoms, an atomically thin graphene layer and an array of metallic wire gate electrodes were configured together into an ultra-compact, thin and flexibly polymeric substrate. The meta-atoms could be designed into hexagonal metallic frames or asymmetric double split rings, which generate Fano like resonances. The metal wire array supplies a quasi-plane electrode to electrically gate the graphene layer for shifting the Fermi level. The graphene layer couples with the near-field of the Fano resonances of the meta-atoms. Hence, variations of graphene's refractive index and absorption would shift and broaden the Fano resonance line shape. By measuring transmission of the terahertz wave through the gate-controlled active graphene metamaterial, the amplitude and phase changes at different V_gs could be calculated, as shown in Fig. 13(d). When V_g was tuned away from the charge neutral point, the resonant frequency redshifts gradually, which is attributed to the increased real part of the complex conductivity of graphene. On the other hand, the linewidth of the resonance become broadened with large V_g due to the Joule losses in the metallic graphene layer. The variation of the on-resonance transmission was estimated as high as 47% (58%) relative to the maximum transmission with the employment of a (multi-layer) graphene monolayer. In addition, the phase change of the graphene metamaterial exceeds 40° at the resonance frequency, which provides possibilities to realize advanced phase-based terahertz devices.

The ability to synthesize and transfer of large scale graphene, as well as graphene's flexibility and integrability, provides a further basis to fabricate complex active terahertz devices. Liang *et al.* monolithically integrated a graphene modulator onto a terahertz quantum cascade laser directly, as shown in Fig. 13(e).[157] This device not only miniaturized the terahertz modulator for improved dynamic speed but also greatly enhanced the modulation depth into a level close to 100% due to the enhanced interaction between graphene and terahertz

radiation. More importantly, the monolithic integration of graphene with the terahertz laser got rid of the optical alignment and the associated bulky mirrors or lenses.

It is also possible to design graphene modulators into an array for realizing a terahertz spatial light modulator. Kakenov *et al.* fabricated a dual graphene layer supercapacitor with an electrolyte as the isolation layer.[158] The top and bottom graphene layers were patterned into ribbons along the perpendicular directions. Thence, the intersections of rows and columns define individually addressable pixels, as schematically shown in Fig. 13(f). By applying a voltage difference between the corresponding row and column, a certain pixel could be addressed, which would block the transmission of the terahertz wave due to graphene's intraband transition. Figure 13(g) displays various spatial modulation patterns with different bias configurations for the terahertz wave at a frequency of 0.37 THz. The broadband operation of the spatial light modulator was estimated as well, showing a flat modulation depth over the frequency range of 0.1–1.5 THz and the modulation depth around 50%. Another similar spatial light modulator was reported by Xing *et al.* in the reflection geometry.[159] An 2D array of graphene squares was patterned onto a substrate of silicon oxide/*p*-silicon. A metal layer was deposited on the backside of the substrate as the reflector and electrode. By applying voltage between the back metal and the individual graphene squares, the reflectance of the incident terahertz wave would be reduced greatly, which gives rise to spatially modulated patterns.

The graphene's Fermi level could also be shifted via a photodoping process with the illumination of an optical beam. The increased carrier concentration supports the intraband transition for absorbing terahertz wave effectively, enabling a high-efficiency all-optical modulator. To realize a considerable doping level of the photo-carriers, visible or infrared pump light are preferred due to the strong interband transition, corresponding to a magnitude of the absorbance of 2.3%. A prototype of the all-optical modulator of terahertz wave is schematically shown in Fig. 14(a).[160] A graphene layer was coated onto a highly doped silicon substrate. A near-infrared pump laser at the wavelength of 780 nm was employed to populate the carriers in graphene and the conducting silicon layer. The probe terahertz beam was launched through the device area pumped by the near-infrared beam, which

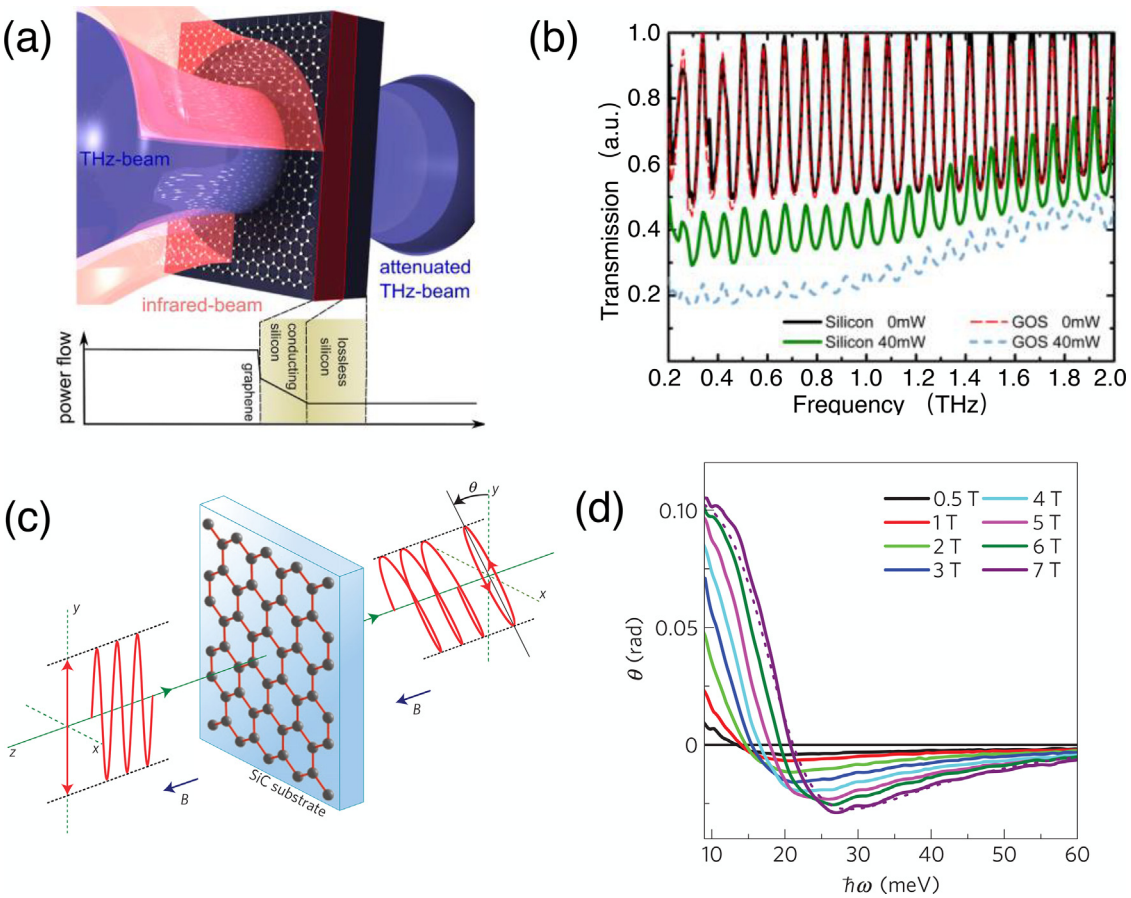

FIG. 14. Graphene-endowed terahertz modulator leveraging all-optical and magneto-optic effects. (a) Schematic representation of an all-optically controlled terahertz modulator by pumping the photocarriers in graphene. (b) All-optical modulation result obtained from the device in (a). (c) Schematic illustration of Faraday rotation to a terahertz radiation when graphene is actuated by a considerable magnetic field. (d) Faraday rotation angle measured under different magnetic fields. (a) and (b) Reproduced with permission from ACS Nano **6**, 9118 (2012). Copyright 2012 American Chemical Society. (c) and (d) Reproduced with permission from Crassee *et al.*, Nat. Phys. **7**, 48 (2011). Copyright 2011 Nature Publishing Group.

would be controlled by the on-off of the pump laser. Here, a doped silicon substrate was chosen for evaluating the modulation effect by graphene. Figure 14(b) displays the modulation results of terahertz beams in the frequency range of 0.2–1 THz by a bare doped silicon substrate and a doped silicon integrated with a graphene layer. Without the pump laser, the transmission spectra have nearly no variations between the terahertz beams transmitting through the bare silicon and graphene-on-silicon. With the illumination of pump laser, transmissions of the terahertz beams after the bare silicon and graphene-on-silicon are both attenuated. However, with the assistance of the graphene monolayer, the modulation depth is increased by ∼20%, giving a modulation depth of ∼72%. Graphene's linear electronic dispersion could not only ensure the modulated terahertz beams in a wide spectral range, but also allow the pump light to be chosen in a broadband optical radiations for photodoping enough carriers.[161,162] Over the past few years, several studies also revealed TMDCs show interesting ultrafast carrier dynamics and terahertz conductivity, which promises the control of terahertz beams optically by integrating them with doped silicons.[163–165]

In conventional bulk materials, the magneto-optic effect is an alternative concept as well for constructing optical modulators with the assistance of polarizers. With the magneto-optic Faraday (Kerr) effect, when a linearly polarized light transmits through (or reflected by) material in the presence of a magnetic field or magnetization, its polarization plane rotates. This phenomenon can be thought of as the "optical-Hall effect" if its origin comes from the conducting electrons or holes. The intrinsically fast magnetization reversal in the magneto-optic effect can go down to a timescale of few tens of femtoseconds. This enables ultrafast modulators if the actuated magnetic fields were fast enough. While modulators based on conventional magneto-optic materials were reported widely,[166] remarkable electronic properties in 2D materials also promise groundbreaking magneto-optic effects for possible optical modulators.

Graphene has the low-energy band structure with a conical dispersion in the effective-mass approximation, which offers interesting physics including half-integer quantum Hall effect. Hence, under a considerable magnetic field, the quantized Hall conductivity in graphene could give rise to a modulated Faraday rotation angle to a terahertz radiation, as schematically shown in Fig. 14(c).[167,168] With a monolayer graphene grown on the silicon carbide substrate, a Faraday rotation angle exceeding 0.1 rad was obtained with a magnetic field up to 7 T at 5 K, as shown in Fig. 14(d). The spectra of rotation angles show a strongly field-dependent edge-like structure, giving rise to a positive rotation angle at low energies and negative angle at high energies. In addition, the Faraday rotation is quantized as well at precisely the quantum Hall steps governed by the Dirac electrons, and the rotation angle is defined by the fine-structure constant. While the maximum Faraday rotation is only 0.1 rad, it is an exceptionally large effect considering graphene's monolayer thickness. As the rotation angle is proportional to the distance traveled by the light, even larger rotation angles were expected from thicker graphene layers.[167,168] Alternatively, giant Faraday rotation in graphene could be remarkably enhanced by constructing resonators[169] or patterning graphene into metasurfaces.[170,171] These unique magneto-optic effects, while are conceptually interesting, may open avenues for constructing terahertz magneto-optic modulators with ultrathin materials under quantum mechanism.

VI. SUMMARIES

In this Review, we have discussed 2D material-endowed optical modulators operating over a spectral range between the visible and terahertz bands, including the underlying material properties, operation mechanisms, and device architectures. Benefiting from the plentiful electronic and optical attributes of 2D materials, the driven effects employed in conventional optical modulators of bulk materials are suitable to them too, including electro-optic, thermo-optic, all-optical, and magneto-optic effects. Note that 2D materials have distinct properties from conventional bulk materials to enable their modulators with advantages. The gapless band structure of graphene with linear dispersion allows the optical responses over the ultraviolet to microwave range. Combining with the easy tunability of the Dirac ferimons, graphene-based optical modulations could be realized in the broad spectral range, representing the widest one in all of the reported optical modulators. In monolayer TMDCs, the internal quantum efficiency of the light–matter interaction is boosted by the tightly bound excitons, which cannot be realized in conventional bulk materials. Modifications of the electronic states in this few atomic layer would be much easier than that in bulk materials, and the power consumption is even lower. From the view of bulk materials, the realization of mid-infrared optical modulators remains challenging due to the requirement of material platforms with versatile optoelectronic properties. Remarkably, few-layer BP with an optical response spectral range between 0.6 and 4 μ could provide strongly field-effect tuned bandgap. Its interband coupling also imbued it with peak-like subband absorption features. Those merits promise BP advantageous in making mid-infrared modulators with low operation voltages.

In the view of integrating modulators into light wave systems, 2D materials' flexibility and dangling-bond-free surface facilitate their modulators to be fabricated on photonic structures. This could get rid of the requirements of complex material growths and etchings involved in the conventional integrated optical modulators. Leveraging the well-developed industry applications of those photonic structures in telecommunication, data communication, and sensing, those integrated 2D material modulators have great potentials to find their realistic applications. For example, in chip-integrated graphene modulators reported by Sorianello *et al.*,[117] device fabrications have been partly included in the standard silicon photonic foundry, paving the way for their low-cost and mass production. Remarkably, from the view of power consumption, operation speed, and extinction ratio, this graphene electro-refractive modulator has advantages over those fabricated from conventional semiconductors.[64]

Here, only the widely studied 2D materials, such as graphene and TMDCs, have been included for reviewing the optical modulators, which already showed potentials for high-quality and large scale growth and transfer.[172–174] These materials have stabilities to allow the device prototype to develop into industries. While BP is considered as an unstable 2D material, the developed packaging techniques could ensure the lifetimes of these electrical and photonic devices.[175,176] There are some other interesting 2D materials, which also support possible functionalities for optical modulations. For example, it has been theoretically demonstrated that the silicene monolayer, a 2D allotrope of silicon, could exhibit an angle of 8° for Faraday rotations in the terahertz regime.[177]

One of another well-known 2D materials is the hexagonal BN that has been recognized as the ideal substrate or dielectric layer for

electrical and photonic devices based on other 2D materials.[178] Because of its wide electronic bandgap (~6 eV), strong light–matter interactions in BN are only expected in the wavelength range of deep ultraviolet (UV).[179–181] The large bandgap also makes it difficult to modify its electronic state for controlling the optical responses in the UV range with the conventional actuation effects, including electrical, magnetic, and all-optical effects. There is still an absence of BN-based optical modulators. Fortunately, BN could supply high quality phonon polariton in the mid-infrared wavelength range relying on its long optical phonon lifetime,[46,47,182] which is well in excess of the highest reported values in the systems of plasmon polariton. In addition, the phonon polariton in BN has the natural optical hyperbolicity,[183,184] enabling its directional propagation with a strong polariton-field enhancement in a waveguide mode. Leveraging on the strong light–matter interactions in the phonon polariton (as schematically indicated in Fig. 1), on-resonance mid-infrared radiation could be effectively modulated by driving 2D BN with an acoustic wave. By patterning the BN layer with nanoribbons, the in-plane dispersion of the phonon polariton could be engineered further to provide more sophisticated degrees in modulating the light field. More importantly, because of the absence of electron–electron scattering, the phonon polariton in BN is immune to Ohmic losses, which is fundamentally distinct from plasmonic systems in graphene or metals. The potentially developed modulators are promising for the mid-infrared spectral range with low insertion loss. Hybridizing BN with other active 2D materials,[46,47] such as graphene and TMDCs, which could be modulated easily with various driven effects, could promise BN-based mid-infrared modulators as well.

In addition, most of the reported 2D material-based optical modulators only include a single material, though the covering spectral range is already very wide. By stacking different 2D materials to form their unconstrained van der Waals heterostructures in virtue of the dangling-bond-free surface between them, the intrinsic electronic structures and light–matter interactions could be modified greatly. This provides alternative architectures for optical modulations. For example, large optical bandgaps of monolayer TMDCs limit their modulators in the visible and near-infrared spectral ranges. By stacking different monolayer TMDCs, the strong interlayer couplings between them could yield robust interlayer excitons with long-lived life and electrical controllability.[185–187] With the band alignment, it is possible to realize interlay excitons of the van der Waals heterostructure with much smaller energy for performing modulators in the long tail of the near-infrared spectral range.[188] On the other hand, the processes of energy transfer and charge transfer in the interlayer of van der Waals heterostructures have possibilities to boost the internal quantum efficiency of light–matter interactions,[189] which could facilitate the improvement of performances in the modulators.

ACKNOWLEDGMENTS

Financial support was provided by the National Key R&D Program of China (Nos. 2018YFA0307200 and 2017YFA0303800), the National Natural Science Foundation of China (No. 91950119), Key Research and Development Program in Shaanxi Province of China (No. 2020JZ-10), and the Fundamental Research Funds for the Central Universities (Nos. 3102017jc01001 and 3102019JC008).

AUTHOR DECLARATIONS

Conflict of Interest

The authors have no conflicts to disclose.

DATA AVAILABILITY

Data sharing is not applicable to this article as no new data were created or analyzed in this study.

REFERENCES

[1]E. L. Wooten, K. M. Kissa, A. Yi-Yan, E. J. Murphy, D. A. Lafaw, P. F. Hallemeier, D. Maack, D. V. Attanasio, D. J. Fritz, G. J. McBrien, and D. E. Bossi, "Review of lithium niobate modulators for fiber-optic communications systems," IEEE J. Sel. Top. Quantum Electron. **6**, 69–82 (2000).
[2]I. P. Kaminow, V. Ramaswamy, R. V. Schmidt, and E. H. Turner, "Lithium niobate ridge waveguide modulator," Appl. Phys. Lett. **24**, 622–624 (1974).
[3]C. Sun, M. T. Wade, Y. Lee, J. S. Orcutt, L. Alloatti, M. S. Georgas, A. S. Waterman, J. M. Shainline, R. R. Avizienis, S. Lin, B. R. Moss, R. Kumar, F. Pavanello, A. H. Atabaki, H. M. Cook, A. J. Ou, J. C. Leu, Y. H. Chen, K. Asanović, R. J. Ram, M. A. Popović, and V. M. Stojanović, "Single-chip microprocessor that communicates directly using light," Nature **528**, 534–538 (2015).
[4]W. Liu, M. Li, R. S. Guzzon, E. J. Norberg, J. S. Parker, M. Lu, L. A. Coldren, and J. Yao, "A fully reconfigurable photonic integrated signal processor," Nat. Photonics **10**, 190–195 (2016).
[5]G. T. Reed, G. Mashanovich, F. Y. Gardes, and D. J. Thomson, "Silicon optical modulators," Nat. Photonics **4**, 518–526 (2010).
[6]F. H. Koppens, T. Mueller, P. Avouris, A. C. Ferrari, M. S. Vitiello, and M. Polini, "Photodetectors based on graphene, other two-dimensional materials and hybrid systems," Nat. Nanotechnol. **9**, 780–793 (2014).
[7]P. Ajayan, P. Kim, and K. Banerjee, "Two-dimensional van der Waals materials," Phys. Today **69**(9), 38–44 (2016).
[8]H. Zhao, Q. Guo, F. Xia, and H. Wang, "Two-dimensional materials for nanophotonics application," Nanophotonics **4**, 128–142 (2015).
[9]K. F. Mak and J. Shan, "Photonics and optoelectronics of 2D semiconductor transition metal dichalcogenides," Nat. Photonics **10**, 216–226 (2016).
[10]F. Barati, M. Grossnickle, S. Su, R. K. Lake, V. Aji, and N. M. Gabor, "Hot carrier-enhanced interlayer electron-hole pair multiplication in 2D semiconductor heterostructure photocells," Nat. Nanotechnol. **12**, 1134–1139 (2017).
[11]C. Li, R. Tian, R. Yi, S. Hu, Y. Chen, Q. Yuan, X. Zhang, Y. Liu, Y. Hao, X. Gan, and J. Zhao, "$MoTe_2$ PN homojunction constructed on a silicon photonic crystal cavity for high-performance photodetector," ACS Photonics **8**, 2431–2439 (2021).
[12]D. Jariwala, A. R. Davoyan, J. Wong, and H. A. Atwater, "Van der Waals materials for atomically-thin photovoltaics: Promise and outlook," ACS Photonics **4**, 2962–2970 (2017).
[13]X. Zhou, X. Hu, J. Yu, S. Liu, Z. Shu, Q. Zhang, H. Li, Y. Ma, H. Xu, and T. Zhai, "2D layered material-based van der Waals heterostructures for optoelectronics," Adv. Funct. Mater. **28**, 1706587 (2018).
[14]R.-J. Shiue, X. Gan, and D. Englund, "On-chip graphene optoelectronic devices for high-speed modulation and photodetection," Proc. SPIE **8994**, 89940P (2014).
[15]K. F. Mak, L. Ju, F. Wang, and T. F. Heinz, "Optical spectroscopy of graphene: From the far infrared to the ultraviolet," Solid State Commun. **152**, 1341–1349 (2012).
[16]D. N. Basov, M. M. Fogler, A. Lanzara, F. Wang, and Y. Zhang, "Colloquium: Graphene spectroscopy," Rev. Mod. Phys. **86**, 959–994 (2014).
[17]C. Gong and X. Zhang, "Two-dimensional magnetic crystals and emergent heterostructure devices," Science **363**, eaav4450 (2019).
[18]Y. Liu, J. Guo, A. Yu, Y. Zhang, J. Kou, K. Zhang, R. Wen, Y. Zhang, J. Zhai, and Z. L. Wang, "Magnetic-induced-piezopotential gated MoS_2 field-effect transistor at room temperature," Adv. Mater. **30**, 1704524 (2018).
[19]G. Plechinger, P. Nagler, A. Arora, A. Granados Del Águila, M. V. Ballottin, T. Frank, P. Steinleitner, M. Gmitra, J. Fabian, P. C. Christianen, R. Bratschitsch, C. Schüller, and T. Korn, "Excitonic valley effects in monolayer

WS_2 under high magnetic fields," Nano Lett. **16**, 7899–7904 (2016), arXiv:1612.03004.
[20]T. Wu and H. Zhang, "Piezoelectricity in two-dimensional materials," Angew. Chem. Int. Ed. **54**, 4432–4434 (2015).
[21]C. Chen, S. Lee, V. V. Deshpande, G. H. Lee, M. Lekas, K. Shepard, and J. Hone, "Graphene mechanical oscillators with tunable frequency," Nat. Nanotechnol. **8**, 923–927 (2013).
[22]D. L. Duong, S. J. Yun, and Y. H. Lee, "Van der Waals layered materials: Opportunities and challenges," ACS Nano **11**, 11803–11830 (2017).
[23]G. R. Bhimanapati, Z. Lin, V. Meunier, Y. Jung, J. Cha, S. Das, D. Xiao, Y. Son, M. S. Strano, V. R. Cooper, L. Liang, S. G. Louie, E. Ringe, W. Zhou, S. S. Kim, R. R. Naik, B. G. Sumpter, H. Terrones, F. Xia, Y. Wang, J. Zhu, D. Akinwande, N. Alem, J. A. Schuller, R. E. Schaak, M. Terrones, and J. A. Robinson, "Recent advances in two-dimensional materials beyond graphene," ACS Nano **9**, 11509–11539 (2015).
[24]B. Deng, V. Tran, Y. Xie, H. Jiang, C. Li, Q. Guo, X. Wang, H. Tian, S. J. Koester, H. Wang, J. J. Cha, Q. Xia, L. Yang, and F. Xia, "Efficient electrical control of thin-film black phosphorus bandgap," Nat. Commun. **8**, 14474 (2017).
[25]M. Xu, T. Liang, M. Shi, and H. Chen, "Graphene-like two-dimensional materials," Chem. Rev. **113**, 3766–3798 (2013).
[26]K. S. Novoselov, A. Mishchenko, A. Carvalho, and A. H. Castro Neto, "2D materials and van der Waals heterostructures," Science **353**, eaac9439 (2016).
[27]F. Xia, H. Wang, D. Xiao, M. Dubey, and A. Ramasubramaniam, "Two-dimensional material nanophotonics," Nat. Photonics **8**, 899–907 (2014).
[28]M. Buscema, D. J. Groenendijk, S. I. Blanter, G. A. Steele, H. S. Van Der Zant, and A. Castellanos-Gomez, "Fast and broadband photoresponse of few-layer black phosphorus field-effect transistors," Nano Lett. **14**, 3347–3352 (2014).
[29]L. Viti, J. Hu, D. Coquillat, W. Knap, A. Tredicucci, A. Politano, and M. S. Vitiello, "Black phosphorus terahertz photodetectors," Adv. Mater. **27**, 5567–5572 (2015).
[30]J. Lu, J. Yang, A. Carvalho, H. Liu, Y. Lu, and C. H. Sow, "Light-matter interactions in phosphorene," Acc. Chem. Res. **49**, 1806–1815 (2016).
[31]K. F. Mak, C. Lee, J. Hone, J. Shan, and T. F. Heinz, "Atomically thin MoS_2: A new direct-gap semiconductor," Phys. Rev. Lett. **105**, 2–5 (2010).
[32]K. F. Mak, J. Shan, and T. F. Heinz, "Electronic structure of few-layer graphene: Experimental demonstration of strong dependence on stacking sequence," Phys. Rev. Lett. **104**, 176404 (2010).
[33]N. Ubrig, E. Ponomarev, J. Zultak, D. Domaretskiy, V. Zólyomi, D. Terry, J. Howarth, I. Gutiérrez-Lezama, A. Zhukov, Z. R. Kudrynskyi, Z. D. Kovalyuk, A. Patané, T. Taniguchi, K. Watanabe, R. V. Gorbachev, V. I. Fal'ko, and A. F. Morpurgo, "Design of van der Waals interfaces for broad-spectrum optoelectronics," Nat. Mater. **19**, 299–304 (2020).
[34]V. Tran, R. Soklaski, Y. Liang, and L. Yang, "Layer-controlled band gap and anisotropic excitons in few-layer black phosphorus," Phys. Rev. B **89**, 235319 (2014).
[35]F. Cui, Q. Feng, J. Hong, R. Wang, Y. Bai, X. Li, D. Liu, Y. Zhou, X. Liang, X. He, Z. Zhang, S. Liu, Z. Lei, Z. Liu, T. Zhai, and H. Xu, "Synthesis of large-size 1T ReS2xSe2(1x) alloy monolayer with tunable bandgap and carrier type," Adv. Mater. **29**, 1705015 (2017).
[36]Y. Liu, Y. Cai, G. Zhang, Y.-W. Zhang, and K.-W. Ang, "Al-doped black phosphorus p-n homojunction diode for high performance photovoltaic," Adv. Funct. Mater. **27**, 1604638 (2017).
[37]Y. Liu, Z. Qiu, A. Carvalho, Y. Bao, H. Xu, S. J. Tan, W. Liu, A. H. Castro Neto, K. P. Loh, and J. Lu, "Gate-tunable giant stark effect in few-layer black phosphorus," Nano Lett. **17**, 1970–1977 (2017).
[38]T. Low, A. S. Rodin, A. Carvalho, Y. Jiang, H. Wang, F. Xia, and A. H. Castro Neto, "Tunable optical properties of multilayer black phosphorus thin films," Phys. Rev. B **90**, 075434 (2014).
[39]M. Liu, X. Yin, E. Ulin-Avila, B. Geng, T. Zentgraf, L. Ju, F. Wang, and X. Zhang, "A graphene-based broadband optical modulator," Nature **474**, 64–67 (2011).
[40]W. Li, B. Chen, C. Meng, W. Fang, Y. Xiao, X. Li, Z. Hu, Y. Xu, L. Tong, H. Wang, W. Liu, J. Bao, and Y. R. Shen, "Ultrafast all-optical graphene modulator," Nano Lett. **14**, 955–959 (2014).
[41]X. Gan, C. Zhao, Y. Wang, D. Mao, L. Fang, L. Han, and J. Zhao, "Graphene-assisted all-fiber phase shifter and switching," Optica **2**, 468 (2015).
[42]Z. Sun, T. Hasan, F. Torrisi, D. Popa, G. Privitera, F. Wang, F. Bonaccorso, D. M. Basko, and A. C. Ferrari, "Graphene mode-locked ultrafast laser," ACS Nano **4**, 803–810 (2010).
[43]M. Tahir and P. Vasilopoulos, "Magneto-optical transport properties of monolayer WSe_2," Phys. Rev. B **94**, 045415 (2016).
[44]H. Da, L. Gao, Y. An, H. Zhang, and X. Yan, "Cavity-induced enhancement of magneto-optic effects in monolayer transition metal dichalcogenides," Adv. Opt. Mater. **6**, 1701175 (2018).
[45]Y. Fang, S. Wu, Z.-Z. Zhu, and G.-Y. Guo, "Large magneto-optical effects and magnetic anisotropy energy in two-dimensional Cr_2Ge_2," Phys. Rev. B **98**, 125416 (2018).
[46]T. Low, A. Chaves, J. D. Caldwell, A. Kumar, N. X. Fang, P. Avouris, T. F. Heinz, F. Guinea, L. Martin-Moreno, and F. Koppens, "Polaritons in layered two-dimensional materials," Nat. Mater. **16**, 182–194 (2017).
[47]D. N. Basov, M. M. Fogler, and F. J. García De Abajo, "Polaritons in van der Waals materials," Science **354**, eaag1992 (2016).
[48]K. F. Mak, M. Y. Sfeir, Y. Wu, C. H. Lui, J. A. Misewich, and T. F. Heinz, "Measurement of the optical conductivity of graphene," Phys. Rev. Lett. **101**, 196405 (2008).
[49]R. R. Nair, P. Blake, A. N. Grigorenko, K. S. Novoselov, T. J. Booth, T. Stauber, N. M. Peres, and A. K. Geim, "Fine structure constant defines visual transparency of graphene," Science **320**, 1308 (2008).
[50]Y. Li, A. Chernikov, X. Zhang, A. Rigosi, H. M. Hill, A. M. van der Zande, D. A. Chenet, E.-M. Shih, J. Hone, and T. F. Heinz, "Measurement of the optical dielectric function of monolayer transition-metal dichalcogenides: MoS_2, $MoSe_2$," Phys. Rev. B **90**, 205422 (2014).
[51]K. F. Mak, K. He, C. Lee, G. H. Lee, J. Hone, T. F. Heinz, and J. Shan, "Tightly bound trions in monolayer MoS_2," Nat. Mater. **12**, 207–211 (2013).
[52]H. L. Liu, C. C. Shen, S. H. Su, C. L. Hsu, M. Y. Li, and L. J. Li, "Optical properties of monolayer transition metal dichalcogenides probed by spectroscopic ellipsometry," Appl. Phys. Lett. **105**, 201905 (2014).
[53]F. Wang, Y. Zhang, C. Tian, C. Girit, A. Zettl, M. Crommie, and Y. R. Shen, "Gate-variable optical transitions in graphene," Science **320**, 206–209 (2008).
[54]Z. Wang, Y.-H. Chiu, K. Honz, K. F. Mak, and J. Shan, "Electrical tuning of interlayer exciton gases in WSe_2 bilayers," Nano Lett. **18**, 137–143 (2018).
[55]A. V. Stier, N. P. Wilson, G. Clark, X. Xu, and S. A. Crooker, "Probing the influence of dielectric environment on excitons in monolayer WSe_2: Insight from high magnetic fields," Nano Lett. **16**, 7054–7060 (2016).
[56]Y. Wang, J. Xiao, H. Zhu, Y. Li, Y. Alsaid, K. Y. Fong, Y. Zhou, S. Wang, W. Shi, Y. Wang, A. Zettl, E. J. Reed, and X. Zhang, "Structural phase transition in monolayer $MoTe_2$ driven by electrostatic doping," Nature **550**, 487–491 (2017).
[57]D. H. Kang, M. H. Jeon, S. K. Jang, W. Y. Choi, K. N. Kim, J. Kim, S. Lee, G. Y. Yeom, and J. H. Park, "Self-assembled layer (SAL)-based doping on black phosphorus (BP) transistor and photodetector," ACS Photonics **4**, 1822–1830 (2017).
[58]S. B. Desai, G. Seol, J. S. Kang, H. Fang, C. Battaglia, R. Kapadia, J. W. Ager, J. Guo, and A. Javey, "Strain-induced indirect to direct bandgap transition in multilayer WSe_2," Nano Lett. **14**, 4592–4597 (2014).
[59]A. P. Nayak, T. Pandey, D. Voiry, J. Liu, S. T. Moran, A. Sharma, C. Tan, C. H. Chen, L. J. Li, M. Chhowalla, J. F. Lin, A. K. Singh, and D. Akinwande, "Pressure-dependent optical and vibrational properties of monolayer molybdenum disulfide," Nano Lett. **15**, 346–353 (2015).
[60]K. Kim, J. Y. Choi, T. Kim, S. H. Cho, and H. J. Chung, "A role for graphene in silicon-based semiconductor devices," Nature **479**, 338–344 (2011).
[61]Y. Liu, N. O. Weiss, X. Duan, H. C. Cheng, Y. Huang, and X. Duan, "Van der Waals heterostructures and devices," Nat. Rev. Mater. **1**, 16042 (2016).
[62]J. Miao, Z. Xu, Q. Li, A. Bowman, S. Zhang, W. Hu, Z. Zhou, and C. Wang, "Vertically stacked and self-encapsulated van der Waals heterojunction diodes using two-dimensional layered semiconductors," ACS Nano **11**, 10472–10479 (2017).
[63]F. Withers, O. Delpozo-Zamudio, A. Mishchenko, A. P. Rooney, A. Gholinia, K. Watanabe, T. Taniguchi, S. J. Haigh, A. K. Geim, A. I. Tartakovskii, and K. S. Novoselov, "Light-emitting engineering heterostructures," Nat. Mater. **14**, 301 (2015).
[64]M. Romagnoli, V. Sorianello, M. Midrio, F. H. Koppens, C. Huyghebaert, D. Neumaier, P. Galli, W. Templ, A. D'Errico, and A. C. Ferrari, "Graphene-

based integrated photonics for next-generation datacom and telecom," Nat. Rev. Mater. **3**, 392–414 (2018).
[65]A. Splendiani, L. Sun, Y. Zhang, T. Li, J. Kim, C. Y. Chim, G. Galli, and F. Wang, "Emerging photoluminescence in monolayer MoS_2," Nano Lett. **10**, 1271–1275 (2010).
[66]O. A. Ajayi, J. V. Ardelean, G. D. Shepard, J. Wang, A. Antony, T. Taniguchi, K. Watanabe, T. F. Heinz, S. Strauf, X.-Y. Zhu, and J. C. Hone, "Approaching the intrinsic photoluminescence linewidth in transition metal dichalcogenide monolayers," 2D Mater. **4**, 031011 (2017).
[67]J. Yang, T. Lü, Y. W. Myint, J. Pei, D. Macdonald, J. C. Zheng, and Y. Lu, "robust excitons and trions in monolayer $MoTe_2$," ACS Nano **9**, 6603–6609 (2015).
[68]B. Radisavljevic, A. Radenovic, J. Brivio, V. Giacometti, and A. Kis, "Single-layer MoS_2 transistors," Nat. Nanotechnol. **6**, 147–150 (2011).
[69]K. F. Mak, K. He, J. Shan, and T. F. Heinz, "Control of valley polarization in monolayer MoS_2 by optical helicity," Nat. Nanotechnol. **7**, 494–498 (2012).
[70]Y. J. Chen, J. D. Cain, T. K. Stanev, V. P. Dravid, and N. P. Stern, "Valley-polarized exciton-polaritons in a monolayer semiconductor," Nat. Photonics **11**, 431–435 (2017).
[71]J. R. Schaibley, H. Yu, G. Clark, P. Rivera, J. S. Ross, K. L. Seyler, W. Yao, and X. Xu, "Valleytronics in 2D materials," Nat. Rev. Mater. **1**, 16055 (2016).
[72]X. Xu, W. Yao, D. Xiao, and T. F. Heinz, "Spin and pseudospins in layered transition metal dichalcogenides," Nat. Phys. **10**, 343–350 (2014).
[73]Y. You, X. X. Zhang, T. C. Berkelbach, M. S. Hybertsen, D. R. Reichman, and T. F. Heinz, "Observation of biexcitons in monolayer WSe_2," Nat. Phys. **11**, 477–481 (2015).
[74]J. S. Ross, S. Wu, H. Yu, N. J. Ghimire, A. M. Jones, G. Aivazian, J. Yan, D. G. Mandrus, D. Xiao, W. Yao, and X. Xu, "Electrical control of neutral and charged excitons in a monolayer semiconductor," Nat. Commun. **4**, 1473–1476 (2013).
[75]S. Dufferwiel, T. P. Lyons, D. D. Solnyshkov, A. A. Trichet, F. Withers, S. Schwarz, G. Malpuech, J. M. Smith, K. S. Novoselov, M. S. Skolnick, D. N. Krizhanovskii, and A. I. Tartakovskii, "Valley-addressable polaritons in atomically thin semiconductors," Nat. Photonics **11**, 497–501 (2017).
[76]H. Zeng, J. Dai, W. Yao, D. Xiao, and X. Cui, "Valley polarization in MoS_2 monolayers by optical pumping," Nat. Nanotechnol. **7**, 490–493 (2012).
[77]T. Cao, G. Wang, W. Han, H. Ye, C. Zhu, J. Shi, Q. Niu, P. Tan, E. Wang, B. Liu, and J. Feng, "Valley-selective circular dichroism of monolayer molybdenum disulphide," Nat. Commun. **3**, 887 (2012).
[78]K. F. Mak, K. L. McGill, J. Park, and P. L. McEuen, "The valley Hall effect in MoS_2 transistors," Science **344**, 1489–1492 (2014).
[79]A. Singh, G. Moody, K. Tran, M. E. Scott, V. Overbeck, G. Berghäuser, J. Schaibley, E. J. Seifert, D. Pleskot, N. M. Gabor, J. Yan, D. G. Mandrus, M. Richter, E. Malic, X. Xu, and X. Li, "Trion formation dynamics in monolayer transition metal dichalcogenides," Phys. Rev. B **93**, 041401 (2016).
[80]B. Li, S. Zu, J. Zhou, Q. Jiang, B. Du, H. Shan, Y. Luo, Z. Liu, X. Zhu, and Z. Fang, "Single-nanoparticle plasmonic electro-optic modulator based on MoS_2 monolayers," ACS Nano **11**, 9720–9727 (2017).
[81]J. Yang, Z. Wang, F. Wang, R. Xu, J. Tao, S. Zhang, Q. Qin, B. Luther-Davies, C. Jagadish, Z. Yu, and Y. Lu, "Atomically thin optical lenses and gratings," Light: Sci. Appl. **5**, e16046 (2016).
[82]G. Scuri, Y. Zhou, A. A. High, D. S. Wild, C. Shu, K. De Greve, L. A. Jauregui, T. Taniguchi, K. Watanabe, P. Kim, M. D. Lukin, and H. Park, "Large excitonic reflectivity of monolayer $MoSe_2$ encapsulated in hexagonal boron nitride," Phys. Rev. Lett. **120**, 37402 (2018).
[83]P. Back, S. Zeytinoglu, A. Ijaz, M. Kroner, and A. Imamoğlu, "Realization of an electrically tunable narrow-bandwidth atomically thin mirror using monolayer $MoSe_2$," Phys. Rev. Lett. **120**, 037401 (2018).
[84]K. F. Mak and J. Shan, "Mirrors made of a single atomic layer," Nature **556**, 177–178 (2018).
[85]D. Krasnozhon, D. Lembke, C. Nyffeler, Y. Leblebici, and A. Kis, "MoS_2 transistors operating at gigahertz frequencies," Nano Lett. **14**, 5905–5911 (2014).
[86]X. Gan, R.-J. Shiue, Y. Gao, S. Assefa, J. Hone, and D. Englund, "Controlled light-matter interaction in graphene electrooptic devices using nanophotonic cavities and waveguides," IEEE J. Sel. Top. Quantum Electron. **20**, 6000311 (2014).
[87]X. Gan, Y. Gao, K. Fai Mak, X. Yao, R.-J. Shiue, A. van der Zande, M. E. Trusheim, F. Hatami, T. F. Heinz, J. Hone, and D. Englund, "Controlling the spontaneous emission rate of monolayer MoS_2 in a photonic crystal nanocavity," Appl. Phys. Lett. **103**, 181119 (2013).
[88]J. R. Piper and S. Fan, "Total absorption in a graphene monolayer in the optical regime by critical coupling with a photonic crystal guided resonance," ACS Photonics **1**, 347–353 (2014).
[89]J. Wang, Z. Cheng, K. Xu, C. Shu, and H. K. Tsang, "Optical absorption and thermal nonlinearities in graphene-on-silicon nitride microring resonators," Asia Commun. Photonics Conf. **27**, 1765–1767 (2015).
[90]H. Fang, J. Liu, H. Li, L. Zhou, L. Liu, J. Li, X. Wang, T. F. Krauss, and Y. Wang, "1305 nm few-layer $MoTe_2$-on-silicon laser-like emission," Laser Photonics Rev. **12**, 1800015 (2018).
[91]I. Datta, S. H. Chae, G. R. Bhatt, M. A. Tadayon, B. Li, Y. Yu, C. Park, J. Park, L. Cao, D. N. Basov, J. Hone, and M. Lipson, "Low-loss composite photonic platform based on 2D semiconductor monolayers," Nat. Photonics **14**, 256–262 (2020).
[92]B. S. Lee, B. Kim, A. P. Freitas, A. Mohanty, Y. Zhu, G. R. Bhatt, J. Hone, and M. Lipson, "High-performance integrated graphene electro-optic modulator at cryogenic temperature," Nanophotonics **10**, 99–104 (2020).
[93]M. Sun, X. Xu, X. W. Sun, X. Liang, V. Valuckas, Y. Zheng, R. Paniagua-Domínguez, and A. I. Kuznetsov, "Efficient visible light modulation based on electrically tunable all dielectric metasurfaces embedded in thin-layer nematic liquid crystals," Sci. Rep. **9**, 8673 (2019).
[94]E. O. Polat and C. Kocabas, "Broadband optical modulators based on graphene supercapacitors," Nano Lett. **13**, 5851–5857 (2013).
[95]Z. Q. Li, E. A. Henriksen, Z. Jiang, Z. Hao, M. C. Martin, P. Kim, H. L. Stormer, and D. N. Basov, "Dirac charge dynamics in graphene by infrared spectroscopy," Nat. Phys. **4**, 532–535 (2008).
[96]H. Li, Y. Anugrah, S. J. Koester, and M. Li, "Optical absorption in graphene integrated on silicon waveguides," Appl. Phys. Lett. **101**, 111110 (2012).
[97]X. Gan, R. J. Shiue, Y. Gao, I. Meric, T. F. Heinz, K. Shepard, J. Hone, S. Assefa, and D. Englund, "Chip-integrated ultrafast graphene photodetector with high responsivity," Nat. Photonics **7**, 883–887 (2013).
[98]S. J. Koester and M. Li, "High-speed waveguide-coupled graphene-on-graphene optical modulators," Appl. Phys. Lett. **100**, 171107 (2012).
[99]Y. Hu, M. Pantouvaki, J. Van Campenhout, S. Brems, I. Asselberghs, C. Huyghebaert, P. Absil, and D. Van Thourhout, "Broadband 10 Gb/s operation of graphene electro-absorption modulator on silicon," Laser Photonics Rev. **10**, 307–316 (2016).
[100]M. Liu, X. Yin, and X. Zhang, "Double-layer graphene optical modulator," Nano Lett. **12**, 1482–1485 (2012).
[101]H. Dalir, Y. Xia, Y. Wang, and X. Zhang, "Athermal broadband graphene optical modulator with 35 GHz speed," ACS Photonics **3**, 1564–1568 (2016).
[102]X. Gan, C. Zhao, Q. Yuan, L. Fang, Y. Li, J. Yin, X. Ma, and J. Zhao, "High performance graphene oxide-based humidity sensor integrated on a photonic crystal cavity," Appl. Phys. Lett. **110**, 151107 (2017).
[103]X. Gan, H. Clevenson, and D. Englund, "Polymer photonic crystal nanocavity for precision strain sensing," ACS Photonics **4**, 1591–1594 (2017).
[104]C. Zhao, Q. Yuan, L. Fang, X. Gan, and J. Zhao, "High-performance humidity sensor based on a polyvinyl alcohol-coated photonic crystal cavity," Opt. Lett. **41**, 5515 (2016).
[105]X. Gan, K. F. Mak, Y. Gao, Y. You, F. Hatami, J. Hone, T. F. Heinz, and D. Englund, "Strong enhancement of light-matter interaction in graphene coupled to a photonic crystal nanocavity," Nano Lett. **12**, 5626–5631 (2012).
[106]X.-T. Gan, C.-Y. Zhao, S.-Q. Hu, T. Wang, Y. Song, J. Li, Q.-H. Zhao, W.-Q. Jie, and J.-L. Zhao, "Microwatts continuous-wave pumped second harmonic generation in few- and mono-layer GaSe," Light: Sci. Appl. **7**, e17126 (2018).
[107]L. Fang, Q. Yuan, H. Fang, X. Gan, J. Li, T. Wang, Q. Zhao, W. Jie, and J. Zhao, "Multiple optical frequency conversions in few-layer GaSe assisted by a photonic crystal cavity," Adv. Opt. Mater. **6**, 1800698 (2018).
[108]X. Gan, R. J. Shiue, Y. Gao, K. F. Mak, X. Yao, L. Li, A. Szep, D. Walker, J. Hone, T. F. Heinz, and D. Englund, "High-contrast electrooptic modulation of a photonic crystal nanocavity by electrical gating of graphene," Nano Lett. **13**, 691–696 (2013).
[109]Y. Gao, R. J. Shiue, X. Gan, L. Li, C. Peng, I. Meric, L. Wang, A. Szep, D. Walker, J. Hone, and D. Englund, "High-speed electro-optic modulator

integrated with graphene-boron nitride heterostructure and photonic crystal nanocavity," Nano Lett. **15**, 2001–2005 (2015).
[110]C. T. Phare, Y. H. Daniel Lee, J. Cardenas, and M. Lipson, "Graphene electro-optic modulator with 30 GHz bandwidth," Nat. Photonics **9**, 511–514 (2015).
[111]C. Qiu, W. Gao, R. Vajtai, P. M. Ajayan, J. Kono, and Q. Xu, "Efficient modulation of 1.55 μm radiation with gated graphene on a silicon microring resonator," Nano Lett. **14**, 6811–6815 (2014).
[112]Y. Ding, X. Zhu, S. Xiao, H. Hu, L. H. Frandsen, N. A. Mortensen, and K. Yvind, "Effective electro-optical modulation with high extinction ratio by a graphene-silicon microring resonator," Nano Lett. **15**, 4393–4400 (2015).
[113]S. A. Mikhailov and K. Ziegler, "New electromagnetic mode in graphene," Phys. Rev. Lett. **99**, 016803 (2007).
[114]V. Sorianello, M. Midrio, and M. Romagnoli, "Design optimization of single and double layer Graphene phase modulators in SOI," Opt. Express **23**, 6478 (2015).
[115]S. W. Ye, F. Yuan, X. H. Zou, M. K. Shah, R. G. Lu, and Y. Liu, "High-speed optical phase modulator based on graphene-silicon waveguide," IEEE J. Sel. Top. Quantum Electron. **23**, 76–80 (2017).
[116]M. Mohsin, D. Neumaier, D. Schall, M. Otto, C. Matheisen, A. Lena Giesecke, A. A. Sagade, and H. Kurz, "Experimental verification of electro-refractive phase modulation in graphene," Sci. Rep. **5**, 10967 (2015).
[117]V. Sorianello, M. Midrio, G. Contestabile, I. Asselberghs, J. Van Campenhout, C. Huyghebaert, I. Goykhman, A. K. Ott, A. C. Ferrari, and M. Romagnoli, "Graphene-silicon phase modulators with gigahertz bandwidth," Nat. Photonics **12**, 40–44 (2018).
[118]H. Li, X. Ma, B. Cui, Y. Wang, C. Zhang, J. Zhao, Z. Zhang, C. Tang, and E. Li, "Chip-scale demonstration of hybrid III-V/silicon photonic integration for an FBG interrogator," Optica **4**, 692 (2017).
[119]J. H. Han, F. Boeuf, J. Fujikata, S. Takahashi, S. Takagi, and M. Takenaka, "Efficient low-loss InGaAsP/Si hybrid MOS optical modulator," Nat. Photonics **11**, 486–490 (2017).
[120]S. Subrina, D. Kotchetkov, and A. A. Balandin, "Heat removal in silicon-on-insulator integrated circuits with graphene lateral heat spreaders," IEEE Electron Device Lett. **30**, 1281–1283 (2009).
[121]S. Gan, C. Cheng, Y. Zhan, B. Huang, X. Gan, S. Li, S. Lin, X. Li, J. Zhao, H. Chen, and Q. Bao, "A highly efficient thermo-optic microring modulator assisted by graphene," Nanoscale **7**, 20249–20255 (2015).
[122]S. Yan, X. Zhu, L. H. Frandsen, S. Xiao, N. A. Mortensen, J. Dong, and Y. Ding, "Slow-light-enhanced energy efficiency for graphene microheaters on silicon photonic crystal waveguides," Nat. Commun. **8**, 14411 (2017).
[123]L. Yu, D. Dai, and S. He, "Graphene-based transparent flexible heat conductor for thermally tuning nanophotonic integrated devices," Appl. Phys. Lett. **105**, 251104 (2014).
[124]Z. Xu, C. Qiu, Y. Yang, Q. Zhu, X. Jiang, Y. Zhang, W. Gao, and Y. Su, "Ultra-compact tunable silicon nanobeam cavity with an energy-efficient graphene micro-heater," Opt. Express **25**, 19479 (2017).
[125]L. Yu, Y. Yin, Y. Shi, D. Dai, and S. He, "Thermally tunable silicon photonic microdisk resonator with transparent graphene nanoheaters," Optica **3**, 159 (2016).
[126]X. Gan, Y. Wang, F. Zhang, C. Zhao, B. Jiang, L. Fang, D. Li, H. Wu, Z. Ren, and J. Zhao, "Graphene-controlled fiber Bragg grating and enabled optical bistability," Opt. Lett. **41**, 603 (2016).
[127]Y. Wang, B. Jiang, S. Das, Q. Zhao, X. Gan, and J. Zhao, "All-optically controlled slow and fast lights in graphene-coated tilted fiber Bragg grating," Appl. Phys. Express **12**, 72010 (2019).
[128]Y. Wang, X. Gan, C. Zhao, L. Fang, D. Mao, Y. Xu, F. Zhang, T. Xi, L. Ren, and J. Zhao, "All-optical control of microfiber resonator by graphene's photothermal effect," Appl. Phys. Lett. **108**, 171905 (2016).
[129]S. Yu, X. Wu, K. Chen, B. Chen, X. Guo, D. Dai, L. Tong, W. Liu, and R. Shen, "All-optical graphene modulator based on optical Kerr phase shift," Optica **3**, 541 (2016).
[130]E. J. Lee, S. Y. Choi, H. Jeong, N. H. Park, W. Yim, M. H. Kim, J. K. Park, S. Son, S. Bae, S. J. Kim, K. Lee, Y. H. Ahn, K. J. Ahn, B. H. Hong, J. Y. Park, F. Rotermund, and D. I. Yeom, "Active control of all-fibre graphene devices with electrical gating," Nat. Commun. **6**, 6851 (2015).
[131]Y. Yao, A. J. Hoffman, and C. F. Gmachl, "Mid-infrared quantum cascade lasers," Nat. Photonics **6**, 432–439 (2012).
[132]A. Lyakh, R. Maulini, A. Tsekoun, R. Go, and C. K. Patel, "Intersubband absorption of quantum cascade laser structures and its application to laser modulation," Appl. Phys. Lett. **92**, 211108 (2008).
[133]K. J. Mitchell, S. Turtaev, M. J. Padgett, T. Čižmár, and D. B. Phillips, "High-speed spatial control of the intensity, phase and polarisation of vector beams using a digital micro-mirror device," Opt. Express **24**, 29269 (2016).
[134]N. Dabidian, S. Dutta-Gupta, I. Kholmanov, K. Lai, F. Lu, J. Lee, M. Jin, S. Trendafilov, A. Khanikaev, B. Fallahazad, E. Tutuc, M. A. Belkin, and G. Shvets, "Experimental demonstration of phase modulation and motion sensing using graphene-integrated metasurfaces," Nano Lett. **16**, 3607–3615 (2016).
[135]B. Zeng, Z. Huang, A. Singh, Y. Yao, A. K. Azad, A. D. Mohite, A. J. Taylor, D. R. Smith, and H.-T. Chen, "Hybrid graphene metasurfaces for high-speed mid-infrared light modulation and single-pixel imaging," Light: Sci. Appl. **7**, 51 (2018).
[136]Y. Yao, R. Shankar, M. A. Kats, Y. Song, J. Kong, M. Loncar, and F. Capasso, "Electrically tunable metasurface perfect absorbers for ultrathin mid-infrared optical modulators," Nano Lett. **14**, 6526–6532 (2014).
[137]D. S. Jessop, S. J. Kindness, L. Xiao, P. Braeuninger-Weimer, H. Lin, Y. Ren, C. X. Ren, S. Hofmann, J. A. Zeitler, H. E. Beere, D. A. Ritchie, and R. Degl'Innocenti, "Graphene based plasmonic terahertz amplitude modulator operating above 100 MHz," Appl. Phys. Lett. **108**, 171101 (2016).
[138]V. W. Brar, M. S. Jang, M. Sherrott, J. J. Lopez, and H. A. Atwater, "Highly confined tunable mid-infrared plasmonics in graphene nanoresonators," Nano Lett. **13**, 2541–2547 (2013).
[139]P. Tassin, T. Koschny, M. Kafesaki, and C. M. Soukoulis, "A comparison of graphene, superconductors and metals as conductors for metamaterials and plasmonics," Nat. Photonics **6**, 259–264 (2012).
[140]R. W. Keyes, "The electrical properties of black phosphorus," Phys. Rev. **92**, 580–584 (1953).
[141]L. Li, Y. Yu, G. J. Ye, Q. Ge, X. Ou, H. Wu, D. Feng, X. H. Chen, and Y. Zhang, "Black phosphorus field-effect transistors," Nat. Nanotechnol. **9**, 372–377 (2014).
[142]F. Xia, H. Wang, and Y. Jia, "Rediscovering black phosphorus as an anisotropic layered material for optoelectronics and electronics," Nat. Commun. **5**, 4458 (2014).
[143]L. Li, J. Kim, C. Jin, G. J. Ye, D. Y. Qiu, F. H. Da Jornada, Z. Shi, L. Chen, Z. Zhang, F. Yang, K. Watanabe, T. Taniguchi, W. Ren, S. G. Louie, X. H. Chen, Y. Zhang, and F. Wang, "Direct observation of the layer-dependent electronic structure in phosphorene," Nat. Nanotechnol. **12**, 21–25 (2017).
[144]X. Wang, A. M. Jones, K. L. Seyler, V. Tran, Y. Jia, H. Zhao, H. Wang, L. Yang, X. Xu, and F. Xia, "Highly anisotropic and robust excitons in monolayer black phosphorus," Nat. Nanotechnol. **10**, 517–521 (2015).
[145]X. Wang and S. Lan, "Optical properties of black phosphorus," Adv. Opt. Photonics **8**, 618 (2016).
[146]G. Zhang, S. Huang, A. Chaves, C. Song, V. O. Özçelik, T. Low, and H. Yan, "Infrared fingerprints of few-layer black phosphorus," Nat. Commun. **8**, 14071 (2017).
[147]C. Lin, R. Grassi, T. Low, and A. S. Helmy, "multilayer black phosphorus as a versatile mid-infrared electro-optic material," Nano Lett. **16**, 1683–1689 (2016).
[148]G. Zhang, A. Chaves, S. Huang, F. Wang, Q. Xing, T. Low, and H. Yan, "Determination of layer-dependent exciton binding energies in few-layer black phosphorus," Sci. Adv. **4**, eaap9977 (2018).
[149]W. S. Whitney, M. C. Sherrott, D. Jariwala, W.-H. Lin, H. A. Bechtel, G. R. Rossman, and H. A. Atwater, "Field effect optoelectronic modulation of quantum-confined carriers in black phosphorus," Nano Lett. **17**, 78–84 (2017).
[150]R. Peng, K. Khaliji, N. Youngblood, R. Grassi, T. Low, and M. Li, "Midinfrared electro-optic modulation in few-layer black phosphorus," Nano Lett. **17**, 6315–6320 (2017).
[151]R. Peng, C. Chen, and M. Li, "Broadband waveguide integrated black phosphorus modulator for mid infrared application," in 2018 Conference on Lasers and Electro-Optics, CLEO 2018 (2018).
[152]H. T. Chen, W. J. Padilla, J. M. Zide, A. C. Gossard, A. J. Taylor, and R. D. Averitt, "Active terahertz metamaterial devices," Nature **444**, 597–600 (2006).

[153]B. Sensale-Rodriguez, T. Fang, R. Yan, M. M. Kelly, D. Jena, L. Liu, and H. Xing, "Unique prospects for graphene-based terahertz modulators," Appl. Phys. Lett. **99**, 113104 (2011).
[154]B. Sensale-Rodriguez, R. Yan, M. M. Kelly, T. Fang, K. Tahy, W. S. Hwang, D. Jena, L. Liu, and H. G. Xing, "Broadband graphene terahertz modulators enabled by intraband transitions," Nat. Commun. **3**, 780–787 (2012).
[155]B. Sensale-Rodriguez, R. Yan, S. Rafique, M. Zhu, W. Li, X. Liang, D. Gundlach, V. Protasenko, M. M. Kelly, D. Jena, L. Liu, and H. G. Xing, "Extraordinary control of terahertz beam reflectance in graphene electro-absorption modulators," Nano Lett. **12**, 4518–4522 (2012).
[156]S. H. Lee, M. Choi, T. T. Kim, S. Lee, M. Liu, X. Yin, H. K. Choi, S. S. Lee, C. G. Choi, S. Y. Choi, X. Zhang, and B. Min, "Switching terahertz waves with gate-controlled active graphene metamaterials," Nat. Mater. **11**, 936–941 (2012).
[157]G. Liang, X. Hu, X. Yu, Y. Shen, L. H. Li, A. G. Davies, E. H. Linfield, H. K. Liang, Y. Zhang, S. F. Yu, and Q. J. Wang, "Integrated terahertz graphene modulator with 100% modulation depth," ACS Photonics **2**, 1559–1566 (2015).
[158]N. Kakenov, T. Takan, V. A. Ozkan, O. Balc i, E. O. Polat, H. Altan, and C. Kocabas, "Graphene-enabled electrically controlled terahertz spatial light modulators," Opt. Lett. **40**, 1984 (2015).
[159]B. Sensale-Rodriguez, S. Rafique, R. Yan, M. Zhu, V. Protasenko, D. Jena, L. Liu, and H. G. Xing, "Terahertz imaging employing graphene modulator arrays," Opt. Express **21**, 2324 (2013).
[160]P. Weis, J. L. Garcia-Pomar, M. Höh, B. Reinhard, A. Brodyanski, and M. Rahm, "Spectrally wide-band terahertz wave modulator based on optically tuned graphene," ACS Nano **6**, 9118–9124 (2012).
[161]Q. Li, Z. Tian, X. Zhang, R. Singh, L. Du, J. Gu, J. Han, and W. Zhang, "Active graphene-silicon hybrid diode for terahertz waves," Nat. Commun. **6**, 7082 (2015).
[162]Z. Chen, X. Chen, L. Tao, K. Chen, M. Long, X. Liu, K. Yan, R. I. Stantchev, E. Pickwell-MacPherson, and J.-B. Xu, "Graphene controlled Brewster angle device for ultra broadband terahertz modulation," Nat. Commun. **9**, 4909 (2018).
[163]Y. Cao, S. Gan, Z. Geng, J. Liu, Y. Yang, Q. Bao, and H. Chen, "Optically tuned terahertz modulator based on annealed multilayer MoS_2," Sci. Rep. **6**, 22899 (2016).
[164]S. Chen, F. Fan, Y. Miao, X. He, K. Zhang, and S. Chang, "Ultrasensitive terahertz modulation by silicon-grown MoS_2 nanosheets," Nanoscale **8**, 4713–4719 (2016).
[165]D.-S. Yang, T. Jiang, and X.-A. Cheng, "Optically controlled terahertz modulator by liquid-exfoliated multilayer WS_2 nanosheets," Opt. Express **25**, 16364 (2017).
[166]S. Kharratian, H. Urey, and M. C. Onbaşli, "Advanced materials and device architectures for magnetooptical spatial light modulators," Adv. Opt. Mater. **8**, 1901381 (2020).
[167]I. Crassee, J. Levallois, A. L. Walter, M. Ostler, A. Bostwick, E. Rotenberg, T. Seyller, D. Van Der Marel, and A. B. Kuzmenko, "Giant Faraday rotation in single- and multilayer graphene," Nat. Phys. **7**, 48–51 (2011).
[168]R. Shimano, G. Yumoto, J. Y. Yoo, R. Matsunaga, S. Tanabe, H. Hibino, T. Morimoto, and H. Aoki, "Quantum Faraday and Kerr rotations in graphene," Nat. Commun. **4**, 1841 (2013).
[169]H.-X. Da and X-h. Yan, "Faraday rotation in bilayer graphene-based integrated microcavity," Opt. Lett. **41**, 151 (2016).
[170]M. Tamagnone, T. M. Slipchenko, C. Moldovan, P. Q. Liu, A. Centeno, H. Hasani, A. Zurutuza, A. M. Ionescu, L. Martin-Moreno, J. Faist, J. R. Mosig, A. B. Kuzmenko, and J.-M. Poumirol, "Magnetoplasmonic enhancement of Faraday rotation in patterned graphene metasurfaces," Phys. Rev. B **97**, 241410 (2018).
[171]A. Dolatabady and N. Granpayeh, "Manipulation of the Faraday rotation by graphene metasurfaces," J. Magn. Magn. Mater. **469**, 231–235 (2019).
[172]L. Gao, G. X. Ni, Y. Liu, B. Liu, A. H. Castro Neto, and K. P. Loh, "Face-to-face transfer of wafer-scale graphene films," Nature **505**, 190–194 (2014).
[173]M. Wang, M. Huang, D. Luo, Y. Li, M. Choe, W. K. Seong, M. Kim, S. Jin, M. Wang, S. Chatterjee, Y. Kwon, Z. Lee, and R. S. Ruoff, "Single-crystal, large-area, fold-free monolayer graphene," Nature **596**, 519–524 (2021).
[174]T. Li, W. Guo, L. Ma, W. Li, Z. Yu, Z. Han, S. Gao, L. Liu, D. Fan, Z. Wang, Y. Yang, W. Lin, Z. Luo, X. Chen, N. Dai, X. Tu, D. Pan, Y. Yao, P. Wang, Y. Nie, J. Wang, Y. Shi, and X. Wang, "Epitaxial growth of wafer-scale molybdenum disulfide semiconductor single crystals on sapphire," Nat. Nanotechnol. **16**, 1201–1207 (2021).
[175]J. Pei, X. Gai, J. Yang, X. Wang, Z. Yu, D.-Y. Choi, B. Luther-Davies, and Y. Lu, "Producing air-stable monolayers of phosphorene and their defect engineering," Nat. Commun. **7**, 10450 (2016).
[176]Z. Wu, Y. Lyu, Y. Zhang, R. Ding, B. Zheng, Z. Yang, S. P. Lau, X. H. Chen, and J. Hao, "Large-scale growth of few-layer two-dimensional black phosphorus," Nat. Mater. **20**, 1203–1209 (2021).
[177]M. Shah and M. S. Anwar, "Magneto-optical effects in the Landau level manifold of 2D lattices with spin-orbit interaction," Opt. Express **27**, 23217 (2019).
[178]C. R. Dean, A. F. Young, I. Meric, C. Lee, L. Wang, S. Sorgenfrei, K. Watanabe, T. Taniguchi, P. Kim, K. L. Shepard, and J. Hone, "Boron nitride substrates for high-quality graphene electronics," Nat. Nanotechnol. **5**, 722–726 (2010).
[179]K. Watanabe, T. Taniguchi, and H. Kanda, "Direct-bandgap properties and evidence for ultraviolet lasing of hexagonal boron nitride single crystal," Nat. Mater. **3**, 404–409 (2004).
[180]J. D. Caldwell, I. Aharonovich, G. Cassabois, J. H. Edgar, B. Gil, and D. N. Basov, "Photonics with hexagonal boron nitride," Nat. Rev. Mater. **4**, 552–567 (2019).
[181]F. Ferreira, A. J. Chaves, N. M. R. Peres, and R. M. Ribeiro, "Excitons in hexagonal boron nitride single-layer: A new platform for polaritonics in the ultraviolet," J. Opt. Soc. Am. B **36**, 674 (2019).
[182]A. J. Giles, S. Dai, I. Vurgaftman, T. Hoffman, S. Liu, L. Lindsay, C. T. Ellis, N. Assefa, I. Chatzakis, T. L. Reinecke, J. G. Tischler, M. M. Fogler, J. H. Edgar, D. N. Basov, and J. D. Caldwell, "Ultralow-loss polaritons in isotopically pure boron nitride," Nat. Mater. **17**, 134–139 (2018).
[183]P. Li, I. Dolado, F. J. Alfaro-Mozaz, F. Casanova, L. E. Hueso, S. Liu, J. H. Edgar, A. Y. Nikitin, S. Vélez, and R. Hillenbrand, "Infrared hyperbolic metasurface based on nanostructured van der Waals materials," Science **359**, 892–896 (2018).
[184]D. Lee, S. So, G. Hu, M. Kim, T. Badloe, H. Cho, J. Kim, H. Kim, C.-W. Qiu, and J. Rho, "Hyperbolic metamaterials: Fusing artificial structures to natural 2D materials," eLight **2**, 1–23 (2022).
[185]H. Fang, C. Battaglia, C. Carraro, S. Nemsak, B. Ozdol, J. S. Kang, H. A. Bechtel, S. B. Desai, F. Kronast, A. A. Unal, G. Conti, C. Conlon, G. K. Palsson, M. C. Martin, A. M. Minor, C. S. Fadley, E. Yablonovitch, R. Maboudian, and A. Javey, "Strong interlayer coupling in van der Waals heterostructures built from single-layer chalcogenides," Proc. Natl. Acad. Sci. U. S. A. **111**, 6198–6202 (2014).
[186]L. A. Jauregui, A. Y. Joe, K. Pistunova, D. S. Wild, A. A. High, Y. Zhou, G. Scuri, K. de Greve, A. Sushko, C. H. Yu, T. Taniguchi, K. Watanabe, D. J. Needleman, M. D. Lukin, H. Park, and P. Kim, "Electrical control of interlayer exciton dynamics in atomically thin heterostructures," Science **366**, 870–875 (2019).
[187]A. Ciarrocchi, D. Unuchek, A. Avsar, K. Watanabe, T. Taniguchi, and A. Kis, "Polarization switching and electrical control of interlayer excitons in two-dimensional van der Waals heterostructures," Nat. Photonics **13**, 131–136 (2019).
[188]S. Latini, K. T. Winther, T. Olsen, and K. S. Thygesen, "Interlayer excitons and band alignment in MoS_2/hBN/WSe_2 van der Waals heterostructures," Nano Lett. **17**, 938–945 (2017).
[189]Y. Chen, Y. Li, Y. Zhao, H. Zhou, and H. Zhu, "Highly efficient hot electron harvesting from graphene before electron-hole thermalization," Sci. Adv. **5**, eaax9958 (2019).